Design and modeling of semiconductor terahertz sources based on nonlinear difference-frequency mixing

by

Alireza Marandi
B.Sc., University of Tehran, 2006

A Thesis Submitted in Partial Fulfillment of the
Requirements for the Degree of

Master of Applied Science

in the Department of Electrical and Computer Engineering

University of Victoria

Design and modeling of semiconductor terahertz sources based on nonlinear difference-frequency mixing

by

Alireza Marandi
B.Sc., University of Tehran, 2006

Supervisory Committee

Prof. Poman P.M. So, Co-Supervisor (ECE Dept.)

Prof. Thomas E. Darcie, Co-Supervisor (ECE Dept.)

Prof. Peter Wild, Outside Member (ME Dept.)

Supervisory Committee

Prof. Poman P.M. So, Co-Supervisor (ECE Dept.)

Prof. Thomas E. Darcie, Co-Supervisor (ECE Dept.)

Prof. Peter Wild, Outside Member (ME Dept.)

Abstract

Unique applications of Terahertz radiation in various fields such as biology and medical sciences, remote sensing, and chemical detection have motivated researchers to develop compact and coherent sources for this least touched region of electromagnetic spectrum. Of the many techniques for generating terahertz signals, difference-frequency generation (DFG) in various crystals is one of the mostly explored methods. Various phase matching methodologies, including phase matching in bulk crystals based on birefringence, and quasi-phase matching have been proposed for this purpose. Although GaAs has an order of magnitude higher second-order nonlinear coefficient in comparison with other crystals, it is one of the least employed crystals for DFG due to phase-matching difficulties. First, it does not provide birefringence in the bulk crystal for birefringence phase matching. Second, GaAs quasi-phase matching has been shown only in few works because patterning the nonlinear susceptibilities in semiconductors is not easily achieved.

In this thesis, integration of a GaAs optical waveguide and a terahertz waveguide is proposed as a wide-band phase matching technique for DFG to generate high

power coherent terahertz radiation. Using waveguides for both optical and terahertz waves allows for tailoring the phase matching and increasing the interaction length to get high conversion efficiency. Using pump wavelengths between 1.5-1.6 μm, where low cost and high optical powers are available, we obtained phase matching for terahertz generation in the range of 0-3.5 THz. We exploit the differences between the GaAs dielectric constant in optical and terahertz range, a high second order nonlinear coefficient, and low terahertz absorption. Simulation results show the appropriate behavior of the proposed devices for both optical and terahertz waves. The proposed waveguide phase matching can be useful for other types of devices using similar nonlinear phenomena, such as coherent detection, electro-optic modulation, and ultra-short pulse generation.

Table of Contents

List of Tables

List of Figures

Chapter 1

Introduction

1.1 Terahertz Radiation

Terahertz mainly refers to the region of electromagnetic spectrum between 300 GHz and 10 THz as depicted in figure 1.1. This range of frequencies lies in between the ranges covered by radio frequency (RF) and microwave techniques, and optical and photonic techniques. It is one of the least touched regions of electromagnetic spectrum due to the lack of efficient and compact sources and components. However, unique applications in several fields such as biology and medical sciences, non-destructive evaluation, and astrophysics have motivated researchers, especially in the last decade, to develop new sources and components for this underused spectral region [10, 11, 12].

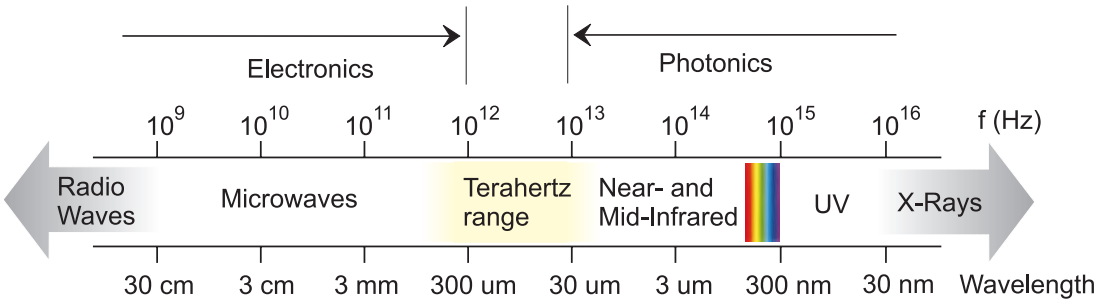

Figure 1.1: Electromagnetic spectrum.

Applications

Promising applications of terahertz waves could be found in many fields. In this section some of those applications in two main categories of terahertz spectroscopy and terahertz imaging are briefly reviewed.

Spectroscopy is known as the measurement of the response of a material to electromagnetic radiation as a function of frequency. Terahertz frequencies are of particular interest because many chemical species have rotational and vibrational absorption in this region and therefore it is a rich spectral range for molecular spectroscopy [13]. Astronomical as well as atmospheric sciences are two areas of interests for terahertz spectroscopy.

A significant fraction of the energy emitted since Big Bang falls into the terahertz range [14, 15]. Therefore, study of this spectral range which is mainly emitted from cool interstellar dust inside galaxies, gives information about star formation and decay [14]. Terahertz radiation received from space also contains information on the cosmic background and distant, newly formed galaxies [16]. Most of submillimeter spectroscopy for space applications has been done on satellite platforms due to the large terahertz absorption of atmosphere. Some applications of terahertz spectroscopy in astronomy could be found in [17, 18].

Terahertz spectroscopy has been also shown to be useful for atmospheric sciences. The chemical processes related to ozone depletion and global warming could be studied according to the thermal emission from gasses such as water, oxygen, and nitrogen compounds [13]. For example, the Earth Observing System (EOS) is a coordinated series of satellites for long-term global observations of the land surface, biosphere, solid Earth, atmosphere, and oceans. In this system terahertz spectroscopy is used at 2.5 THz to monitor the OH level of the atmosphere [19].

Terahertz imaging for the first time reported in [20] and has since developed significantly and has attracted many researchers in both academia and industry. It

is usually performed using ultra-short terahertz pulses generated by optical ultra-short pulses interacting with photoconductors or nonlinear crystals [21]. Reflected or transmitted pulses are detected and image information is extracted from the phase and amplitude of the received signal. Terahertz frequencies are of specific interest because many materials that are opaque in visible optical range are transparent in this region. Medical imaging of teeth or sub-dermal melanoma [22, 23], and security imaging of concealed weapons [24] are examples of this type of imaging.

Applications of terahertz waves are not limited to the reported examples in this thesis and more examples and references could be found [10, 11, 12].

1.2 Terahertz Generation Techniques

Due to some fundamental issues, extension of the frequency range of existing electronic or optical sources to the terahertz range is not easily achievable. Solid-state electronic devices such as transistors, Gunn oscillators and Schottky diode multipliers are not efficient at frequencies much higher that 100 GHz due to high frequency roll-off resulting from carrier transit time and resistance-capacitance effects [10]. On the other hand, direct generation of such a long wavelength in a laser is limited by lack of appropriate material with a small bandgap (1-10 THz $\rightarrow$ 1-40 meV) [10].

However, many techniques have been developed to generate radiation at frequencies above 1 THz. These techniques can be classified into three main categories: microwave up-convertors, optical down-convertors, and terahertz lasers. Terahertz generated by up-conversion of microwave to the terahertz range can be done with low efficiency via chains of Schottky doublers or triplers [25]. Optical down-conversion for terahertz generation can be obtained using optical nonlinearity or photoconductivity by applying optical short pulses for generation of terahertz pulses or two optical wavelengths for continuous-wave terahertz generation [26]. Terahertz lasers are realized with optically pumped molecular gas lasers [27], free electron lasers [28], or

quantum cascade lasers [29]. Although many of these sources are very useful, each of the has its own benefits and disadvantages and the search for a perfect terahertz source continues. Excellent overviews of them could be found in [10, 11, 12]. In this section two classes of the most popular terahertz sources: quantum cascade lasers, and photo-mixers, are briefly reviewed.

Quantum Cascade Lasers

Quantum cascade lasers are first demonstrated in 1994 at Bell Laboratories [30]. In the conventional laser diodes, electromagnetic radiation is emitted through the recombination of electron-hole pairs across the material band gap. However, in quantum cascade lasers, laser emission is achieved through the use of intersubband transitions in a periodic repetition of layers of two different compositions, or superlattice structure [30]. The supperlattice structure could be also defined as a periodic structure of quantum wells and barriers. The photon energy resulted from an intersubband transition in such a structure can be specified by the thicknesses of the coupled wells and barriers. Therefore, these structures can be used to generate long wavelength radiation. Although the idea of intersubband emission was known since 1971 [31], the enabling crystal growth technology for creating quantum cascade lasers is relatively new and expensive. Molecular beam epitaxy (MBE), in which individual monolayers can be grown, provides the required precision [32]. Many quantum cascade lasers are reported recently working in the terahertz range [29].

So far, terahertz quantum cascade lasers have been realized to generate radiation in the range of 1.2-5 THz with powers up to tens of mW [29]. Two main disadvantages of these terahertz sources are their poor beam patterns and low working temperature. One of the highest working temperatures is 160 K for 3 THz operation [33].

Photo-Mixers

Photomixers are the most common terahertz sources and are commercially available up to 2 THz with output power in μW range [10, 11]. The CW generation of high frequency radiation by photomixing is based on generating carriers in a semiconductor by two lasers emitting at nearly the same wavelengths, but detuned by the terahertz frequency. The beating of two incident frequencies will modulate the carrier density in the crystal, and therefore the conductivity between the contacts covering the material. If these photogenerated carriers are subjected to a DC electric field applied between two contacts, a THz current is induced that can be connected to an antenna to radiate. The ultra-short terahertz pulses could also be generated from the carrier density modulation by applying ultra-short optical pulses to the photo-mixer.

Photomixer-based terahertz sources are limited in frequency due to the carrier recombination lifetime and carrier transit time or mobility in semiconductors. Low temperature grown GaAs is one of the mostly used material for terahertz photomixers [34] which has a recombination lifetime of 130 fs corresponding to 3 dB frequency of 1.2 THz. While highly suitable and readily available for efficient operation up to this frequency, extending operation to multiple terahertz remains a challenge and new materials are proposed for this purpose [26].

1.3 Our Approach

The main focus of this thesis is terahertz generation using difference-frequency mixing in GaAs. GaAs is a desirable material for this application as it has a very high second-order nonlinear coefficient and low terahertz absorption [35, 1]. Two incident optical wavelengths generate terahertz radiation due to difference-frequency generation (DFG), a well-known nonlinear effect that has been used for terahertz generation in several configurations (as will be discussed in chapter 3). Unlike photomixers, DFG is not limited in frequency and has potentially better performance for higher frequen-

cies. However, demonstrated DFG-based terahertz generators need to be excited by high power pulsed lasers, use complicated setups for phase matching, and usually work for a narrow-band terahertz range only. In this thesis we are seeking a waveguide device that can be used as an efficient continuous-wave DFG-based terahertz source while using the widely available lasers and optical amplifiers that have been developed for telecommunication applications.

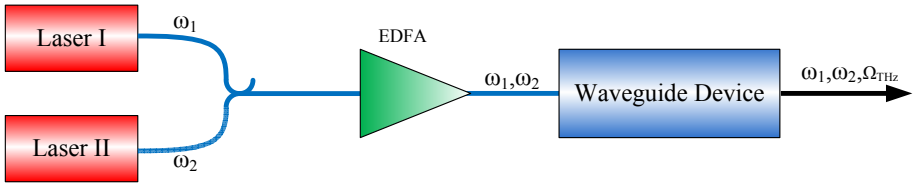

Figure 1.2: Schematic diagram of a setup for generating terahertz radiation using the proposed devices in this thesis.

A schematic diagram of the ideal setup for generating terahertz signals using the proposed device in this thesis is depicted in figure 1.2. Two tunable lasers working at frequencies of ω_1 and ω_2 are coupled to an Erbium-doped fiber amplifier (EDFA) and then applied to the device which generates the terahertz radiation.

The waveguide device is a combination of an optical and a terahertz waveguide in the same structure. This device is designed to provide appropriate condition for the efficient nonlinear interaction of the incident beams. This requires high overlap between the optical and terahertz modes, and appropriate mode velocities that result in a phase matching condition for the nonlinear process. By using waveguide structures, not only can the phase-matching of the process be tailored, but also the interaction length and therefore the conversion efficiency can be increased.

The schematic diagram of the frequencies, and DFG process is depicted in figure 1.3. As depicted in this figure, the output terahertz frequency (Ω_{THz}) is tuned by the difference-frequency of ω_1 and ω_2. However, to provide phase matching for the DFG process, the position of the frequencies, i.e. the average frequency, should be tuned or selected to satisfy the phase matching condition for the desired terahertz

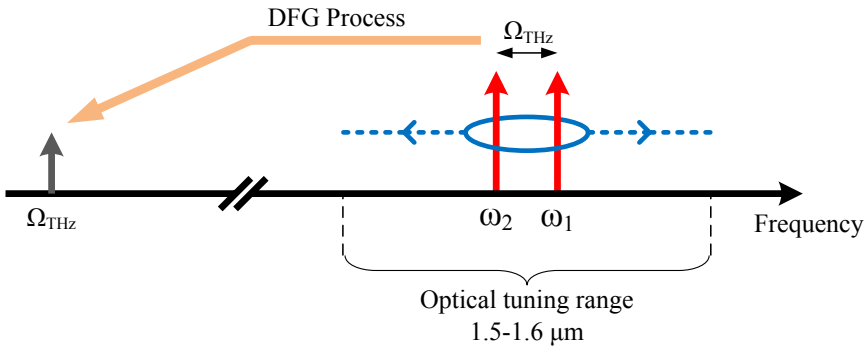

Figure 1.3: Schematic diagram of terahertz generation using a DFG process.

frequency.

The main constraint for this design is the limit on the range of optical frequencies available from lasers and optical amplifiers. Low cost distributed-feedback (DFB) lasers are tunable over a few nanometers and extended cavity or fiber lasers are tunable over tens of nanometers all within 1.5-1.6 μm. Therefore, the optical tuning range for the optical wavelengths is 1.5-1.6 μm and the waveguide device should provide phase matching for the DFG process involving two incident wavelengths in this range and their terahertz difference-frequency.

1.4 Thesis Overview

In this thesis, the high second-order nonlinearity of GaAs is exploited to generate terahertz radiation by difference-frequency mixing. The difference between the dielectric constants of GaAs in optical and terahertz ranges enables phase-matching of the DFG process in the proposed waveguide structures. Simulation results and analytical studies of the proposed structures show promising performance of these structures for coherent tunable terahertz sources.

In the next chapter of this thesis the theory of nonlinear optics in waveguide structures is reviewed. The equations for terahertz generation based on DFG process are derived and discussed. In the third chapter, related background techniques and devices are discussed, including nonlinear fibers, all-optical wavelength convertors,

optical modulators, and nonlinear terahertz generators. The fourth chapter provides information about the material properties and waveguide characteristics that are used in this thesis. The fifth chapter describes our proposed devices for DFG-based terahertz generation with the comprehensive study of each. Chapter six describes a new FDTD-based simulation tool for modeling the nonlinear behavior of guided waves. In chapter seven we summarize the work and provide future prospects for this project and approach. Appendix A briefly overviews the simulation tools used in the numerical analysis. CST Microwave Studio is used to obtain the electromagnetic properties of the waveguide structures, and analytical calculations are used to predict the nonlinear behavior.

Chapter 2

Nonlinear Guided Wave Interactions

2.1 Introduction

Nonlinear optics generally refers to the study of the phenomena that occur as a result of the modification of optical properties of a material system by the presence of light. These phenomena happen regularly at sufficiently high intensities provided by lasers. The beginning of nonlinear optics goes back to the discovery of second-harmonic generation by Franken *et al.* in 1961 [36], shortly after invention of lasers in 1960. After that, a wide range of research has been done to study different nonlinear behavior of materials and to design new optical and electro-optical devices based on nonlinear optics [1, 37, 38].

In this thesis, we are interested in second-order nonlinearity in crystals, especially GaAs. This effect is used to generate electromagnetic waves in the terahertz regime using difference-frequency generation (DFG). Our analysis is based on Maxwell's equations and the nonlinear susceptibility tensor.

This chapter starts with an overview of nonlinear optics theory and associated Maxwell's equations. Difference-frequency generation is then studied and the relevant equations are derived based on the nonlinear wave equation. After that, nonlinear interactions in waveguides are studied briefly. Finally, DFG-based terahertz generation is discussed comprehensively.

2.2 Nonlinear Optics Theory

Nonlinear interactions of electromagnetic waves could be explained by well-known Maxwell's curl equations [37]:

$$\mu \frac{\partial \vec{H}}{\partial t} = -\nabla \times \vec{E}, \tag{2.1}$$

and

$$\frac{\partial \vec{D}}{\partial t} + \sigma \vec{E} = \nabla \times \vec{H}, \tag{2.2}$$

where σ and μ are electric conductivity and permeability of the material, respectively. $\vec{D}$ is the electric flux density vector. In the presence of nonlinear polarization it can be written as:

$$\vec{D} = \varepsilon_0 \varepsilon_r \vec{E} + \vec{P}^{(NL)}. \tag{2.3}$$

The first term is the linear flux density determined by free space permittivity (ε_0) and relative permittivity ($\varepsilon_r = 1 + \chi_e$), which is a scalar for an isotropic material and is a second rank tensor for an anisotropic medium. $\vec{P}^{(NL)}$ is the induced nonlinear polarization, which depends nonlinearly on the electric field strength. Therefore, equation 2.2 in the presence of nonlinear polarization would be:

$$\varepsilon_0 \varepsilon_r \frac{\partial \vec{E}}{\partial t} + \sigma \vec{E} + \frac{\partial \vec{P}^{(NL)}}{\partial t} = \nabla \times \vec{H}. \tag{2.4}$$

Combination of equations 2.1 and 2.4 results in the nonlinear wave equation:

$$\nabla^2 \vec{E} = \mu\sigma \frac{\partial \vec{E}}{\partial t} + \mu\epsilon \frac{\partial^2 \vec{E}}{\partial t^2} + \mu \frac{\partial^2 \vec{P}^{(NL)}}{\partial t^2}. \tag{2.5}$$

For second-order nonlinear interactions, which are the main focus of this thesis, the nonlinear polarization vector could be determined in its vector form according

to the second-order nonlinear susceptibility tensor ($[d_{ij}]$) and electric field strength. The spatial relationship is:

$$\vec{P}^{(2)} = \begin{pmatrix} d_{11} & d_{12} & d_{13} & d_{14} & d_{15} & d_{16} \\ d_{21} & d_{22} & d_{23} & d_{24} & d_{25} & d_{26} \\ d_{31} & d_{32} & d_{33} & d_{34} & d_{35} & d_{36} \end{pmatrix} \times \begin{pmatrix} E_x^2 \\ E_y^2 \\ E_z^2 \\ E_y E_z \\ E_x E_z \\ E_y E_x \end{pmatrix}. \tag{2.6}$$

This equation shows that the induced second-order polarization depends on the $[d_{ij}]$ tensor of a material. This tensor depends on molecular and crystalline structure of the media. Crystals are classified into different groups based on the structure of this tensor. For example, GaAs is in the $\overline{4}3m$ group in which $d_{14} = d_{25} = d_{36}$ while other components are zero. On the other hand, nonlinear susceptibility tensors of materials are usually reported based on the crystallographic axes, which means that in order to use equation 2.6 the electric field in physical coordinate system should be transformed to the crystallographic coordinate system according to the crystal cut.

Different second-order nonlinear processes can be explained by using equations 2.6 and 2.5. The last term of the right side of equation 2.5 can act as a source of new frequencies. For example, when two incident frequencies of ω_1 and ω_2 are applied, the terms E_xE_y, E_xE_z, or E_zE_y in equation 2.6 are able to produce new frequencies of $(\omega_1 - \omega_2)$ and/or $(\omega_1 + \omega_2)$. These processes are known as difference-frequency generation and sum-frequency generation, respectively. Moreover, if there is a single incident frequency of ω_1, the terms E_x^2, E_y^2, or E_z^2 in equation 2.6 can produce a new frequency of $2\omega_1$ which is known as second-harmonic generation. The schematic diagrams of these processes are shown in figures 2.1.

The vector form of nonlinear wave equation shows how the field components

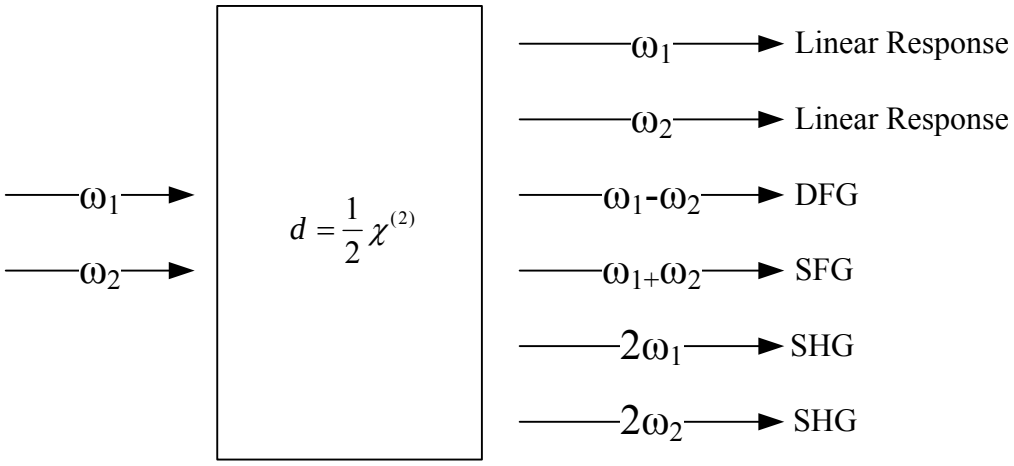

Figure 2.1: Second-order nonlinear processes: Difference-Frequency Generation (DFG), Sum-Frequency Generation (SFG), and Second-Harmonic Generation (SHG).

interact in three dimensions. To study the second-order nonlinear interactions in one dimension, it is assumed that the $\vec{P}^{(2)}$ is parallel to $\vec{E}$. This case is not only easy to analyze but it is also appropriate for the GaAs-based devices considered in this thesis. The properties of GaAs that will result in such a behavior is discussed in later chapters. Therefore, the simplified scalar form of wave equation in 2.5 for second-order nonlinear interaction would be:

$$\nabla^2 E = \mu\sigma\frac{\partial E}{\partial t} + \mu\epsilon\frac{\partial^2 E}{\partial t^2} + \mu\frac{\partial^2 P^{(2)}}{\partial t^2}. \tag{2.7}$$

We limit our calculations to three plane waves of frequencies ω_1, ω_2, and ω_3 propagating in z direction:

$$E^{(\omega_1)}(z,t) = Re\{E_1(z)e^{j(\omega_1 t - k_1 z)}\}, \tag{2.8a}$$

$$E^{(\omega_2)}(z,t) = Re\{E_2(z)e^{j(\omega_2 t - k_2 z)}\}, \tag{2.8b}$$

$$E^{(\omega_3)}(z,t) = Re\{E_3(z)e^{j(\omega_3 t - k_3 z)}\}, \tag{2.8c}$$

and

$$E = E^{(\omega_1)}(z,t) + E^{(\omega_2)}(z,t) + E^{(\omega_3)}(z,t). \tag{2.9}$$

For the second order nonlinear polarization we have:

$$P^{(2)} = dE^2. \tag{2.10}$$

where d is the second-order nonlinear coefficient, i.e. the scalar form of the second-order susceptibility tensor.

This induced polarization contains terms of:

$$Re\{dE_1E_2e^{j((\omega_1-\omega_2)t-(k_1-k_2)z)}\},$$

and

$$Re\{dE_2E_3e^{j((\omega_2+\omega_3)t-(k_2+k_3)z)}\},$$

which oscillate at new frequencies of $(\omega_1 - \omega_2)$ and $(\omega_2 + \omega_3)$. These terms in order to oscillate at any of the frequencies : ω_1, ω_2, and ω_3 should satisfy the following equation:

$$\omega_1 = \omega_2 + \omega_3. \tag{2.11}$$

Therefore, the term at $(\omega_1 - \omega_2)$ will oscillate at ω_3, which is DFG, and the term at $(\omega_2 + \omega_3)$ will oscillate at ω_1, which is SFG. Equation 2.11 could also be derived from conservation of energy. For example, in DFG, a photon at higher frequency of ω_1 produces two photons at lower frequencies of ω_2 and ω_3. This equation states that the sum of the energies of the produced photons is equal to the energy of the first photon.

To derive the relationship between the amplitudes of these frequencies and find the coupling between them, the fields in equation 2.8 is substituted into equation 2.7

and the slowly varying envelope condition is assumed:

$$\left| k_l \frac{dE_l(z)}{dz} \right| \gg \left| \frac{d^2 E_l(z)}{dz^2} \right| , l = 1, 2, 3.$$

Therefore, for each frequency the following differential equations are obtained showing the dependence of each amplitude on itself and coupling between other frequencies:

$$\frac{dE_3}{dz} = -\frac{\sigma_3}{2}\sqrt{\frac{\mu}{\varepsilon_3}}E_3 - \frac{j\omega_3}{2}\sqrt{\frac{\mu}{\varepsilon_3}}dE_1E_2^*e^{-j(k_1-k_2-k_3)z}, \tag{2.12a}$$

$$\frac{dE_2^*}{dz} = -\frac{\sigma_2}{2}\sqrt{\frac{\mu}{\varepsilon_2}}E_2 + \frac{j\omega_2}{2}\sqrt{\frac{\mu}{\varepsilon_2}}dE_3E_1^*e^{-j(k_3-k_1+k_2)z}, \tag{2.12b}$$

$$\frac{dE_1}{dz} = -\frac{\sigma_1}{2}\sqrt{\frac{\mu}{\varepsilon_1}}E_1 - \frac{j\omega_1}{2}\sqrt{\frac{\mu}{\varepsilon_1}}dE_3E_2e^{-j(k_3+k_2-k_1)z}. \tag{2.12c}$$

These equations can be used to explain the second-order nonlinear interactions containing three frequencies of ω_1, ω_2, and ω_3. In the next section the focus is on difference-frequency generation. This process is also known as parametric amplification in the sense that the signal at ω_2 is amplified by the nonlinear process, and an idler wave is generated at ω_3. If the whole process occurs in a resonant structure at ω_3 and/or ω_2, oscillation will occur as a result of the gain of the parametric amplification. This structure is known as a parametric oscillator. We will use the term difference-frequency generation for our terahertz generation because both incident optical frequencies exist and we are interested in the generated signal which is in the terahertz regime.

2.3 Difference-Frequency Generation

For convenience, the equations 2.12 is rearrenged to the simpler form of:

$$\frac{dA_3}{dz} = -\frac{1}{2}\alpha_3 A_3 - \frac{j}{2}\kappa A_1 A_2^* e^{-j(\Delta k)z}, \tag{2.13a}$$

$$\frac{dA_2^*}{dz} = -\frac{1}{2}\alpha_2 A_2 + \frac{j}{2}\kappa A_3 A_1^* e^{j(\Delta k)z}, \tag{2.13b}$$

$$\frac{dA_1}{dz} = -\frac{1}{2}\alpha_1 A_1 - \frac{j}{2}\kappa A_3 A_2 e^{j(\Delta k)z}, \tag{2.13c}$$

by the following definitions [37]:

$$A_l \equiv \sqrt{\frac{n_l}{\omega_l}} E_l, l = 1, 2, 3, \tag{2.14a}$$

$$\Delta k \equiv k_1 - k_2 - k_3, \tag{2.14b}$$

$$\kappa \equiv d\sqrt{\left(\frac{\mu}{\varepsilon_0}\right)\frac{\omega_1\omega_2\omega_3}{n_1 n_2 n_3}}, \tag{2.14c}$$

$$\alpha_l \equiv \sigma_l \sqrt{\frac{\mu}{\varepsilon_l}}, l = 1, 2, 3. \tag{2.14d}$$

where A_l is normalized amplitude (according to the square-route of frequency) and n_1, n_2, and n_3 are the refractive indices of the wave in the material at ω_1, ω_2, and ω_3.

It is assumed that the power transformed from the wave at ω_1 by the other frequencies ω_2 and ω_3 is negligible compared to the power at ω_1, i.e. $A_1(z)$ is constant along the interaction length and pump depletion is ignored. Moreover, no material loss ($\sigma_l = 0$) is assumed. Therefore, the solutions to equations 2.14 would be:

$$A_3(z) = \left[A_3(0)\left(\cosh\left(\frac{g}{2}z\right) - \frac{j\Delta k}{g}\sinh\left(\frac{g}{2}z\right)\right) - jA_2^*(0)\sinh\left(\frac{g}{2}z\right)\right] e^{j\frac{\Delta k}{2}z} \tag{2.15}$$

and

$$A_2(z) = \left[A_2^*(0)\left(\cosh\left(\frac{g}{2}z\right) - \frac{j\Delta k}{g}\sinh\left(\frac{g}{2}z\right)\right) + jA_3(0)\sinh\left(\frac{g}{2}z\right)\right] e^{j\frac{\Delta k}{2}z}, \tag{2.16}$$

where $A_3(0) = A_3(z=0)$, $A_2(0) = A_2(z=0)$, $A_3(0) = A_3^*(0)$, and

$$g \equiv \sqrt{\frac{\mu\omega_3\omega_2}{\varepsilon_0 n_1 n_2} d^2 E_1(0)^2 - \left(\frac{\Delta k}{2}\right)^2}.$$

In these equations, $\Delta k = k_1 - k_2 - k_3$ is known as wave-number mismatch, and has an important effect on the efficiency of the nonlinear processes. For the phase matched conditions where $\Delta k = 0$, equations 2.15 and 2.16 become:

$$A_3(z) = A_3(0)\cosh\left(\frac{g}{2}z\right) - jA_2^*(0)\sinh\left(\frac{g}{2}z\right) \tag{2.17}$$

and

$$A_2^*(z) = A_2^*(0)\cosh\left(\frac{g}{2}z\right) + jA_3(0)\sinh\left(\frac{g}{2}z\right). \tag{2.18}$$

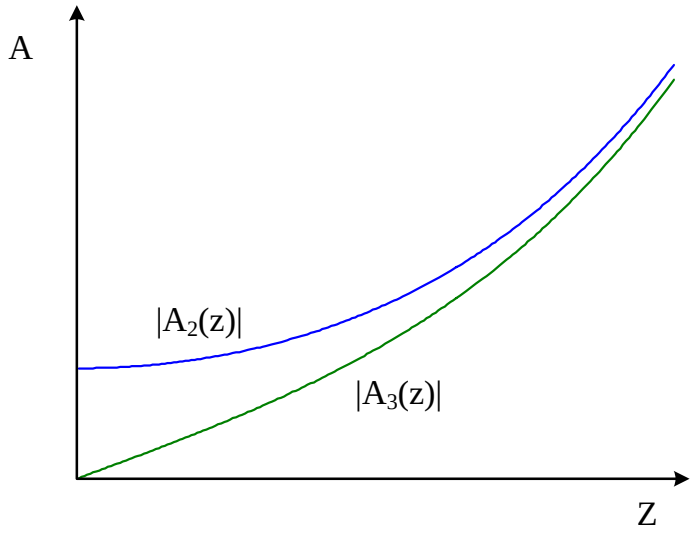

Figure 2.2: Evolution of A_3 and A_2 on the way of interaction (z) for a phase-matched environment ($\Delta k = 0$).

Figure 2.2 shows the evolution of the amplitudes along the interaction length (z) for phase-matched conditions. The amplified signal (A_2) increases as a cosh function and the generated signal increases as sinh. Figure 2.3 compares the evolution of the

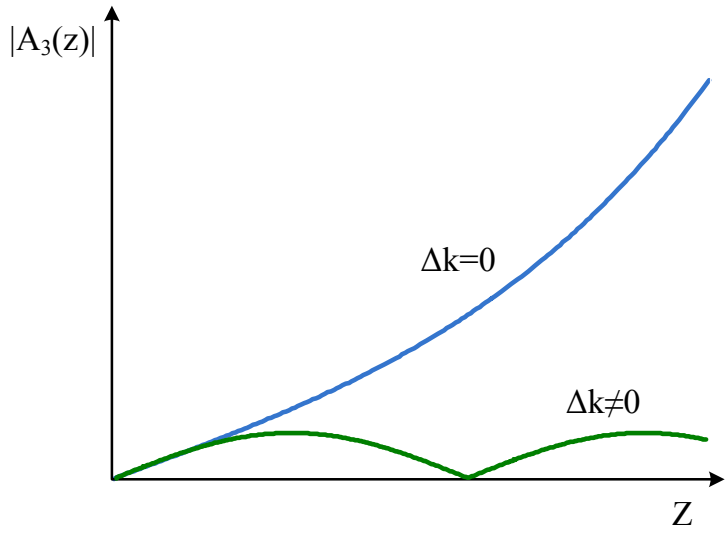

Figure 2.3: Evolution of A_3 on the way of interaction (z) for a phase matched ($\Delta k = 0$) and non-phase matched ($\Delta k \neq 0$) environments.

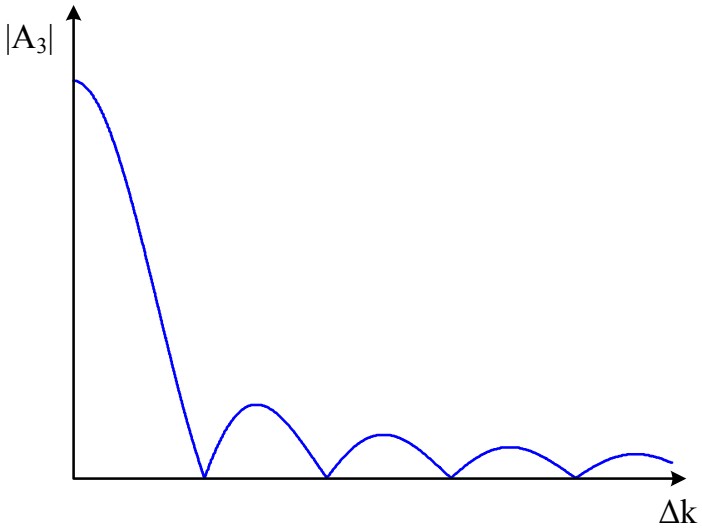

Figure 2.4: Effects of wave-vector mismatch (Δk) on the generated amplitude (A_3).

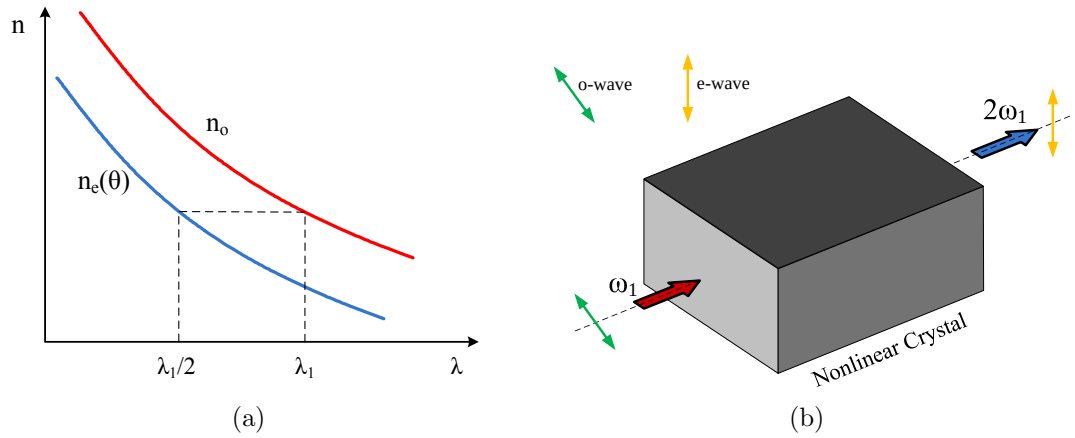

Figure 2.5: Birefringence phase matching, (a) dispersion of the refractive index of ordinary and extraordinary waves in a negative uniaxial crystal, (b) schematic of angle-tuning for birefringence phase matching .

generated signal at ω_3 in the two cases of perfect phase matching ($\Delta k = 0$) and non-phase matched condition ($\Delta k \neq 0$). In this figure the non-phase matched plot is for the case that g is an imaginary number. Therefore, the sinh function in equation 2.17 become a sin function. And in this case, instead of having the flow of energy from the higher frequency to the lower frequencies by way of the nonlinear interaction, it bounces back and forth and consequently the DFG process becomes inefficient. The effect of wave-number mismatch on the generated amplitude at a constant length is also depicted in figure 2.4.

2.3.1 Phase Matching Techniques

In order to achieve efficient wavelength conversion, phase matching between interaction waves is required. In this section we review three of the most common ways of phase matching techniques, i.e. birefringence phase matching, quasi-phase matching, and waveguide phase matching.

Birefringence Phase Matching

One of the phase matching techniques that has been used widely [1] involves satisfying the phase matching condition ($\Delta k = 0$) by taking advantage of the natural

birefringence of anisotropic crystals. For example for second-harmonic generation the phase matching condition would be [37]:

$$k_{2\omega_1} = 2k_{\omega_1} \Rightarrow n_{2\omega_1} = n_{\omega_1}. \tag{2.19}$$

Under certain circumstances, this condition could be satisfied when two frequencies have different polarizations. In birefringent crystals, the refractive index of two perpendicular polarizations are different. Therefore, it is often possible to find polarization angles to compensate the refractive index difference of two frequencies. For example, figure 2.5(a) shows the changes of the refractive indices of two polarizations known as ordinary (n_o) and extraordinary ($n_e(\theta)$) with angle of θ versus the wavelength for a negative uniaxial crystal ($n_e < n_o$). In this case, the refractive index of the ordinary wave at λ_1 could be matched to the refractive index of extraordinary wave at $\lambda_1/2$. Therefore, as depicted in figure 2.5(b), by tuning the angle of the incident polarization (or the crystal angle) the phase matching criteria for second harmonic generation could be met. Some examples of birefringence phase matching for DFG-based processes are reported in [39, 40].

However, birefringence phase matching is limited to birefringent crystals where the interacting wavelengths correspond to material transparency. In addition, the presence of both ordinary and extraordinary polarized radiations usually results in divergence of the generated wave from the incident wave during the propagation in the material. This is known as birefringence walk-off [1], a phenomenon that limits the conversion efficiency of birefringence phase-matched nonlinear processes.

Quasi-Phase Matching

Quasi-phase matching allows a positive net flow of energy from the pump frequency to the signal and idler frequencies by creating a periodic changes in the nonlinear orientation from the medium. Momentum conservation is obtained through an ad-

ditional momentum contribution of the wavevector of the periodic structure. More details about the theory of quasi-phase matching could be found in [1, 37], and some examples of using this technique are reported in [41, 42, 8].

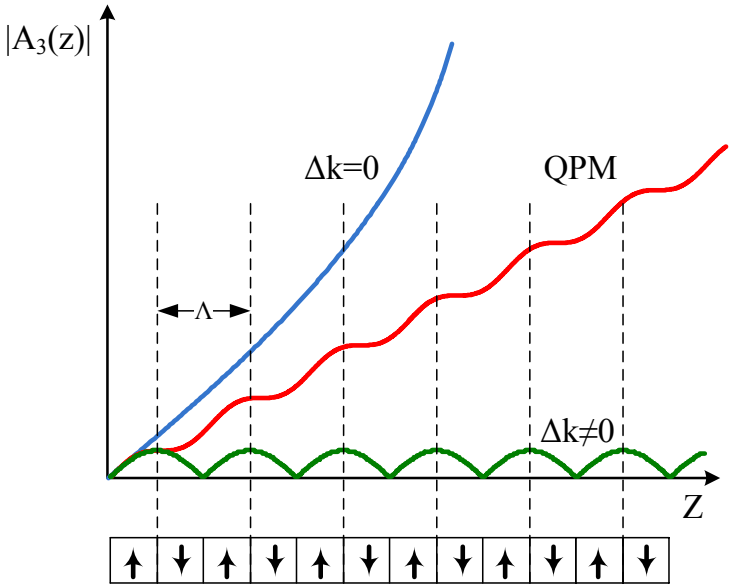

Figure 2.6: A periodically poled material for quasi-phase-matching in which the nonlinear orientation alternatively changes with period of Λ, and the generated amplitude of the DFG process for three cases of phase-matched ($\Delta k = 0$), non-phase-matched ($\Delta k \neq 0$) and quasi-phase-matched (QPM).

Figure 2.6 shows a comparison between the evolution of the generated amplitude in DFG process for three cases of perfectly phase matched, quasi-phase matched, and non-phase matched processes along with the periodic changes of the nonlinear orientation of the crystal.

Waveguide Phase Matching

Waveguide phase matching is a general term to describe when phase matching for an optical nonlinear process is provided using a waveguide structure. Different waveguide structures have been used to enable or enhance the efficiency of nonlinear effects in different material such as optical fibers, photonic crystals, and slow-wave structures.

In optical fibers, nonlinear effects have been enhanced by tailoring the refractive index distributions of the fibers. Examples of this kind of structures are reported

in [38]. Photonic crystal fibers are another type of waveguides that has been used to provide phase-matching for the nonlinear interactions [43]. Also, for an optical polarization modulator, a combination of a dielectric slab waveguide and slow wave coplanar electrode structure has been used to match the velocity of optical and microwave waves to allow efficient nonlinear electro-optical interaction [44]. This device and some other waveguide structures for nonlinear processes are studied in the next chapter.

GaAs has a very high second-order nonlinear coefficient. However, it does not provide birefringence in bulk crystal, so birefringence phase matching is not possible. Moreover, patterning the nonlinear orientation of semiconductors is challenging therefore, quasi-phase matching is difficult in GaA [45]. In this thesis we use a new approach to provide phase-matching for DFG process in GaAs using waveguide structures.

2.4 Nonlinear Optics in Waveguides

To study nonlinear interactions of guided waves, it is necessary to modify the equations presented in section 2.2, which are for plane waves. For each guided mode of the waveguide we have two-dimensional field distributions $(\vec{E}(x,y), \vec{H}(x,y))$ and some other properties such as mode effective index and mode loss. Rather than using refractive index, wave-number, and conductivity of the plane waves in equations 2.14, the characteristics of the modes are used (we consider single mode propagation at each frequency): where c is the speed of light in free space. These values for a guided

$$\begin{array}{rc} \text{The effective index of the mode at } \omega_l\text{:} & n_l^{eff}\ , \\ \text{Effective wave-number of the mode at } \omega_l\text{:} & k_l^{eff} = \frac{n_l^{eff}\omega_l}{c}\ , \\ \text{Loss of the mode at } \omega_l\text{:} & \alpha_l^{eff}\ , \end{array}$$

mode could be calculated either analytically for simple waveguide structures [46] or obtained using simulation tools.

To define the relationship between the power guided by a mode and amplitude of the mode, we have:

$$\frac{P_l}{A_l^{eff}} = \frac{1}{2}\sqrt{\frac{\varepsilon_0}{\mu}}\omega_l |A_l|^2, \tag{2.20}$$

where A_l^{eff} is the effective area of the mode at ω_l which could be calculated according to the electric field distribution of the corresponding mode ($\vec{E}(x,y)$) by the following equation:

$$A_l^{eff} \equiv \frac{\int\int |\vec{E}_l(x,y)|^2 dxdy}{max(|\vec{E}_l(x,y)|)^2}. \tag{2.21}$$

Based on this definition, A_l, which could be calculated from the modified forms of the equations 2.15 and 2.16, corresponds to the maximum magnitude of the electric field of the corresponding mode.

The last modification to the nonlinear equations is for d, the second-order nonlinear coefficient. According to [47], this value can be modified according to the overlap between the modes:

$$\Gamma = \frac{\int\int |\vec{E}_1(x,y)||\vec{E}_2(x,y)||\vec{E}_3(x,y)| dxdy}{\left(\int\int |\vec{E}_1(x,y)| dxdy\right)\left(\int\int |\vec{E}_2(x,y)| dxdy\right)\left(\int\int |\vec{E}_3(x,y)| dxdy\right)}. \tag{2.22}$$

This overlap factor (Γ) describes how different modes can interact with each other, and therefore the second-order coefficient can be modified as:

$$d_{eff} = \Gamma d. \tag{2.23}$$

In the next section these modifications are used to calculate the terahertz output power of a DFG process.

2.5 DFG-Based Terahertz Generation

The schematic view of DFG-based terahertz generation is depicted in figure 2.7. In this case, two optical frequencies of ω_1 and ω_2 are applied to a second-order nonlinear material, and the difference-frequency of the input frequencies is generated due to difference-frequency generation.

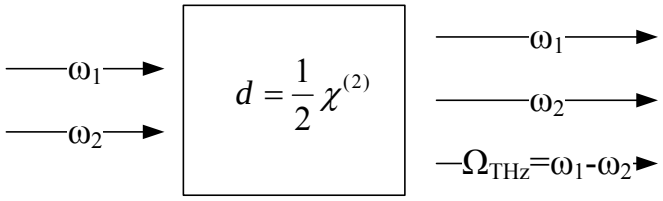

Figure 2.7: Terahertz generation by DFG.

In this process the generated terahertz frequency would be:

$$\Omega_{THz} = \omega_1 - \omega_2, \tag{2.24}$$

which satisfies the energy conservation of the involved photons. Also, for the momentum conservation, which is the phase matching condition, we have:

$$k_{THz} = k_1 - k_2, \tag{2.25}$$

where k_1, k_2, and k_{THz} are the corresponding wave numbers on the way of propagation. Dividing these two equations results in:

$$\frac{\Omega_{THz}}{k_{THz}} = \frac{\omega_1 - \omega_2}{k_1 - k_2}. \tag{2.26}$$

Assuming that the difference between optical frequencies is very small, (i.e. in our case it is terahertz vs. optical), and also the similar situation for the wave numbers, equation 2.26 can be rewritten as:

$$\frac{\Omega_{THz}}{k_{THz}} \simeq \frac{d\omega_{optical}}{dk_{optical}}. \tag{2.27}$$

This means that the phase matching for terahertz generation could be represented as:

$$v_{THz}^{ph} = v_{optical}^{gr}, \tag{2.28}$$

where v_{THz}^{ph} is the phase velocity of terahertz wave and $v_{optical}^{gr}$ is the group velocity of the optical signal. Therefore, in terms of the indices we have:

$$n_{THz}^{ph} = n_{optical}^{gr}, \tag{2.29}$$

where n_{THz}^{ph} is the phase index or the effective index of the terahertz wave and $n_{optical}^{gr}$ is the group index of the optical wave. In this thesis, the group index or group velocity of an optical signal containing two close optical frequencies of ω_1, ω_2 means the group index or group velocity of the wave at the average optical frequency of: $(\frac{\omega_1+\omega_2}{2})$.

The representation of the phase matching condition in terms of group and phase velocities makes sense physically by considering that the velocity of the optical envelope should be equal to the velocity of the generated terahertz wave in order to add up constructively during propagation.

2.5.1 Terahertz Generation in Waveguides

To derive the output terahertz power in terms of incident optical powers in a DFG-based terahertz generation in a waveguide structure, we use the equations presented in section 2.3 modified as discussed in section 2.4.

In our application high powers are used for incident at pump frequencies of ω_1 and ω_2, and it is considered that pump depletion and amplification are negligible.

Moreover, because we are working with very low material and waveguide losses, as it is discussed in next chapters, the losses is neglected ($\alpha_l = 0$) and therefore, equations 2.13 become:

$$\frac{dA_3}{dz} = -\frac{j}{2}\kappa A_1 A_2^* e^{-j(\Delta k)z}, \tag{2.30a}$$

$$\frac{dA_2^*}{dz} = 0, \text{ and} \tag{2.30b}$$

$$\frac{dA_1}{dz} = 0. \tag{2.30c}$$

Since ω_1 and ω_2 are relatively close to each other, the same material and waveguide properties for both pumps can be considered. From now on, the index "optical" on a variable means that we are using the same value for both optical frequencies for that variable. For the terahertz frequency we use "THz" index. The solution to equations 2.30 for the perfectly phase matched condition ($\Delta k = 0$) is :

$$A_3 = -\frac{j}{2}\kappa A_1(0) A_2^*(0) z. \tag{2.31}$$

Therefore, for the magnitude of the generated terahertz wave we have:

$$|A_3| = |\frac{\kappa}{2}||A_1(0)||A_2(0)|z. \tag{2.32}$$

According to equation 2.20, the relationship between the power (P_l) and amplitude (A_l) for optical range is:

$$|A_{1,2}| = \sqrt{\frac{2P_{1,2}}{A_{1,2}^{eff}\omega_{1,2}}\sqrt{\frac{\mu}{\varepsilon_0}}},$$

where $A_{1,2}^{eff}$ is the effective area of the optical waveguide mode which can be calculated from

$$A_{optical}^{eff} \equiv A_{1,2}^{eff} = \frac{\int\int |\vec{E}_{optical}(x,y)|^2 dxdy}{max(|\vec{E}_{optical}(x,y)|)^2}.$$

And for the terahertz mode,

$$|A_{THz}| \equiv |A_3| = \sqrt{\frac{2P_{THz}}{A_{THz}^{eff}\omega_{1,2}}\sqrt{\frac{\mu}{\varepsilon_0}}}$$

where

$$A_{THz}^{eff} \equiv \frac{\int\int |\vec{E}_{THz}(x,y)|^2 dxdy}{max(|\vec{E}_{THz}(x,y)|)^2}.$$

The other value needed to calculate output terahertz power is the effective second-order coefficient ($d_{eff} = \Gamma d$), and according to equation 2.22:

$$\Gamma = \frac{\int\int |\vec{E}_{THz}(x,y)||\vec{E}_{optical}(x,y)|^2 dxdy}{\left(\int\int |\vec{E}_{THz}(x,y)|dxdy\right)\left(\int\int |\vec{E}_{optical}|^2 dxdy\right)}. \tag{2.33}$$

Therefore, we can find out the output terahertz power (P_{THz}) in terms of input optical powers (P_1, P_2) for a perfect phase-matching, considering no material loss, and assuming that the input powers are much higher than the generated power:

$$P_{THz} = 2\frac{A_{THz}^{eff}}{\left(A_{optical}^{eff}\right)^2} d_{eff}^2 \left(\frac{\mu}{\varepsilon_0}\right)^{3/2} \frac{P_1 P_2 \Omega_{THz}^2}{n_1 n_2 n_{THz}} z^2. \tag{2.34}$$

In this equation, increasing the effective area of the terahertz mode (A_{THz}^{eff}) and decreasing that of the optical mode ($A_{optical}^{eff}$) will increase the output power. However, it should be considered that this will significantly decrease the overlap factor (Γ) and consequently d_{eff}. Also from equation 2.34, the effects of mode overlap and optical effective area are squared compared to effective terahertz area. Therefore, in our

design we will try to increase the overlap and decrease the optical mode area to get higher output powers.

The other obvious conclusion that can be made is that the dependence of the output power on the terahertz frequency shows that the higher the difference-frequency of the optical wavelengths, the higher the output power. This was also predictable considering the one-to-one photon conversion in the process where two optical photons generate one terahertz photon. Therefore, for the same photon conversion efficiency, the higher frequency terahertz photon would have higher energy. This is also one of the main advantages of DFG-based terahertz generation over photo-mixing techniques, for which the efficiency decreases with increasing the frequency.

Chapter 3

Related Work

3.1 Introduction

In this chapter we review previously proposed nonlinear optics devices that generate new frequencies that do not exist in the incident fields. First, we review some of the proposed devices for nonlinear interactions in optical range. In section 3.2, enhancement of nonlinear effects in dispersion flattened fibers are reviewed. It is shown that the waveguide structures, i.e. fiber core pattern in this case, can improve the nonlinear effects in the fiber by providing phase matching. We also review the concept of all-optical wavelength conversion and one of the proposed conversion techniques based on second-order nonlinear interactions in section 3.3. In these two sections all incident and generated frequencies are in the optical range. After that, we discuss the nonlinear effects in which at least one of the involved frequencies is not in the optical range. Two types of optical beam modulators are discussed in section 3.4, and section 3.5 describes terahertz generation based on nonlinear processes. Some of the recently proposed terahertz generators are studied. Finally, the distinction between our approach and previously discovered approaches for nonlinear terahertz generation are discussed.

3.2 Nonlinear Fibers

In optical fiber communications, nonlinear effects are one of the limiting factors of the communication link performance. However, many of those effects have been used for several useful applications such as optical amplifiers, fiber lasers, and wavelength converters [38]. Most optical fibers are not good second-order nonlinear media, but do exhibit other nonlinear effects such as four-wave mixing (third-order nonlinearity), Beryllium and Raman effects. In this section, some of the proposed highly nonlinear fiber structures are studied to illustrate how the waveguide structures can increase the efficiency of the nonlinear processes. Specifically, new frequencies are generated through third-order nonlinear processes ($\chi^{(3)}$) involving two relatively close incident frequencies of ω_1 and ω_2, resulting in frequencies $2\omega_1 - \omega_2$ or $2\omega_2 - \omega_1$ that are still close to the incident frequencies.

One of the early types of fibers showed high nonlinear effects is known as dispersion flattened fiber. The core design of such fibers results in a very low dispersion over a wide range of wavelengths (usually 1.3-1.6 μm) [48]. Therefore, in this type of fibers, the velocities of different wavelengths are very close to each other which means phase matching could be satisfied for many nonlinear processes. The main approach to provide such situation in fibers is tailoring their refractive index profile. Figure 3.1 shows one of the early proposals for a flat dispersion fiber [2]. The frequency-dependent distribution of the mode, results in a waveguide (modal) dispersion which can cancel out the material dispersion and provides net dispersion of close to zero over a wide range as depicted in figure 3.2. In this figure, the dashed and solid curves illustrate waveguide dispersion and total dispersion, respectively. The dotted-dashed curve is for a regular single mode fiber, and circles are for material. This figure shows how different values of Δ affect the waveguide dispersion.

This kind of fibers have been used widely for many nonlinear applications for

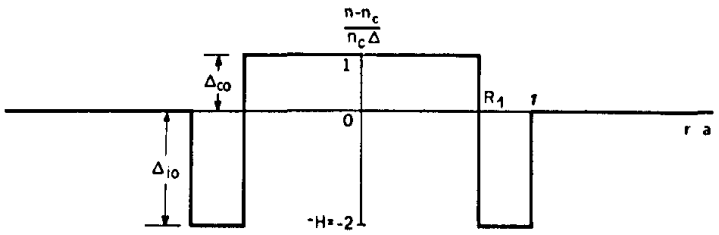

Figure 3.1: Refractive index profile of a double-clad fiber which results in a flat dispersion. Figure is reprinted from [2].

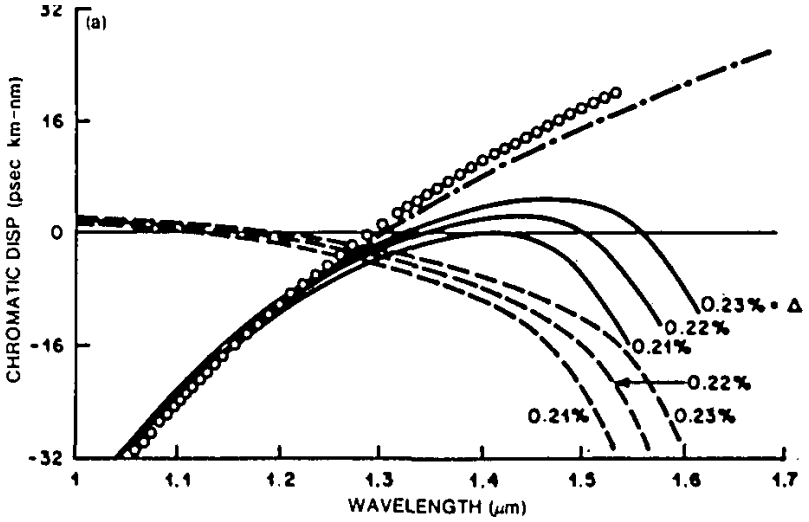

Figure 3.2: Dispersion spectra for double-clad fibers of figure 3.1 with 2a = 13 μm and $\Delta = 0.21\%, 0.22\%, 0.23\%$. Figure is reprinted from [2].

decades [38], such as quasi-tuable wavelength conversion within the whole C-band [49]. In this work, four-wave mixing inside the fiber is used to change the wavelength of the signal in the range of 1530-1565 nm.

Photonic crystal fibers [43] are another relatively new development and have been used widely for nonlinear applications. The main idea to improve the nonlinearities is the same as early nonlinear fibers, which is tailoring the refractive index profile, but in this case in a more complex form of two dimensional. One of the examples of this type of fibers used for nonlinear applications is an extruded photonic crystal fiber shown in figure 3.3 [3]. The fiber has zero group velocity dispersion at wavelengths around 1550 nm, and approximately an order of magnitude higher nonlinearity than comparable silica fibers. Generation of an ultra-broad super-continuum of 350 nm to 2200 nm using a 1550 nm ultrafast pump source is demonstrated by this fiber in [3].

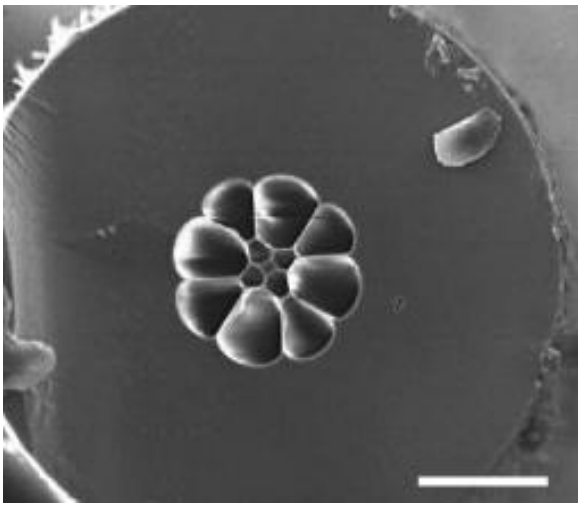

Figure 3.3: Cross section of a photonic crystal fiber used for super-continuum generation formed from commercial SF6 glass (bar, 10 μ m). Figure is reprinted from [3].

3.3 All-Optical Wavelength Converters

Another example of a device that generates signals at new frequencies through a nonlinear process is the all-optical wavelength converter. These are potentially important devices for all-optical networks, where they can change the carrier wavelength

of a channel in a Wavelength Division Multiplexing (WDM) network . Wavelength conversion is realized using either $\chi^{(3)}$ processes in nonlinear fibers or $\chi^{(2)}$ processes in second-order nonlinear devices [50]. In this section, we study one of the recently proposed methods of all-optical wavelength conversion using second-order processes in a periodically poled lithium niobate device [4].

Figure 3.4 shows the scheme of a tunable wavelength conversion based on cascaded SFG and DFG processes. An optical signal modulated on an optical frequency of f_{signal} with two continuous-wave pump beams of P1 and P2 at f_{pump1} and f_{pump2} are applied to the device. Through the interaction of the signal and P1, an SFG wave is generated under a quasi-phase-matched condition. A converted signal is obtained by DFG between the SFG wave and the pump P2. Since the converted frequency is given by:

$$f_{converted} = f_{SFG} - f_{pump2} \tag{3.1}$$

The converted signal could be tuned by tuning the frequency of P2 [4]. In this reference, error-free tunable wavelength conversion with a bit-error-rate of less than 10^{-9} for a 160-Gb/s return to zero optical signal over a 23-nm tuning range is demonstrated. The signal and P1 wavelength were 1552.0 and 1544.7 nm, the SFG signal was generated at 774.6 nm, and 160-Gb/s converted signals were generated at 1562.0 and 1539.0 nm by setting the wavelength of P2 to 1536.0 and 1559.0 nm, respectively.

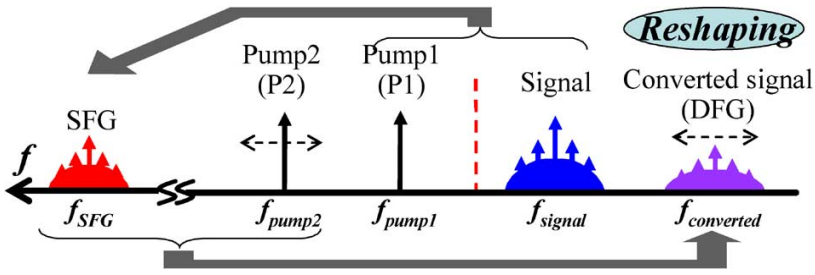

Figure 3.4: Schematic diagram of tunable wavelength conversion in PPLN based on cSFG-DFG with spectral reshaping. Figure is reprinted from [4].

3.4 Optical Modulators

Optical modulators are devices that have been used extensively to modulate an optical beam with a radio frequency signal [51]. They are one of the main building blocks of optical communication networks, due to the limitations of direct modulation of laser diodes. In this section we review two optical modulator structures. The first structure is a combination of an optical waveguide and a slow-wave coplanar structure in which the velocities of the optical and microwave signals are matched to allow for an efficient electro-optical interaction. The second structure is a quantum cascade laser which generates a terahertz signal and the generated signal is then used to modulate an incident optical beam in the same structure using second-order nonlinear processes. Both of these structures are important for us, as they provide phase matching between optical and microwave (or terahertz) signals.

Slow-Wave Coplanar Electrode - Slab

Slow-wave coplanar electrode structures are one of many types of millimeter-wave waveguides that have been used on top of dielectric slab waveguides in several applications [44, 5, 52, 53]. We are particularly interested in the polarization modulator described in [44]. This structure has been also used to generate microwave radiation by optical rectification [52]. The frequency-dependent behavior of the structure is suitable for the velocity-matching of an RF signal up to 40GHz with an optical beam at 1550 nm.

Figure 3.5 shows the structure of this optical polarization modulator. The velocity of the modulating electric signal guided by the slow-wave coplanar structure is matched to the velocity of the optical signal guided by the ridged slab waveguide. The fins and pads are used to add capacitance to the line without changing the inductance, which reduces the phase velocity of microwave signal, i.e. increases the microwave index. Figure 3.6 shows the resultant microwave index along with the

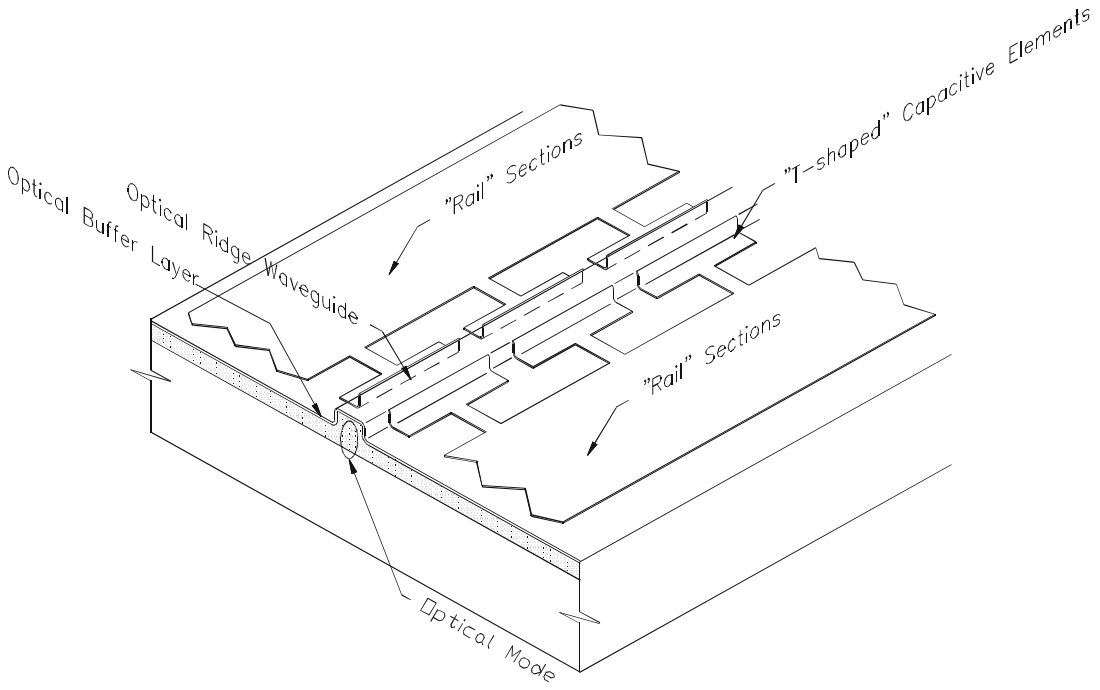

Figure 3.5: Slow-wave coplanar structure on top of an optical waveguide as an optical modulator. Figure is reprinted from [5].

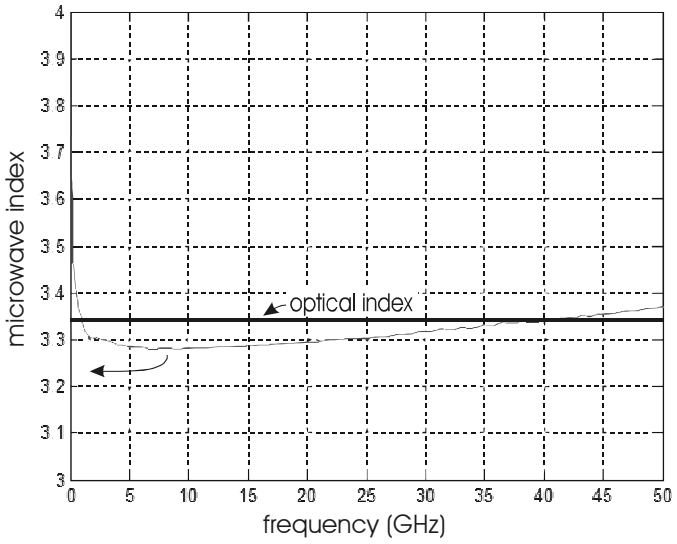

Figure 3.6: Microwave index of the device depicted in figure 3.5. Figure is reprinted from [5].

optical index which is constant around 1550 nm.

The same structure has been used to detect the microwave signal modulated on an optical beam in [52] using second-order nonlinear processes in the device. The output power of the generated signal (about -95 dBm at 10 GHz when the input optical power is 15 dBm) is very close to the calculated values due to the phase matching provided in the structure. Another similar structure has been also used to generate ultra-short electric pulses by rectification of optical pulses due to the second-order nonlinear process in [53].

Modulation of an Optical Beam with a Terahertz Signal

One of the state-of-the-art optical modulation techniques is reported in [6]. The structure is a combination of a parallel-plate waveguide for a terahertz wave and a dielectric slab waveguide for an optical beam. The GaAs dielectric used in the waveguide structure contains the active region of a quantum cascade laser, which generates a single frequency terahertz wave. Due to second-order nonlinearity in the crystal, the terahertz signal is modulated on an incident optical beam. In the devices for terahertz generation proposed in this thesis a similar structure is proposed (section 5.2).

The phase matching of the optical and terahertz wave is obtained by varying the width of the structure for different wavelengths. Figure 3.7 shows the optical signal at 1.56 μm and generated sidebands with a terahertz frequency of 2.8 THz which is generated by the quantum cascade laser. These sidebands are generated by DFG ($\omega_{telecom} - \Omega_{THz}$) and SFG ($\omega_{telecom} + \Omega_{THz}$) in GaAs. The width of the device is 47 μm and the laser is cooled to 10 K for continuous wave operation.

3.5 Nonlinear THz Generators

In the first chapter of this thesis we reviewed different types of terahertz sources such as photo-mixers, quantum cascade lasers and nonlinear terahertz generators. In this

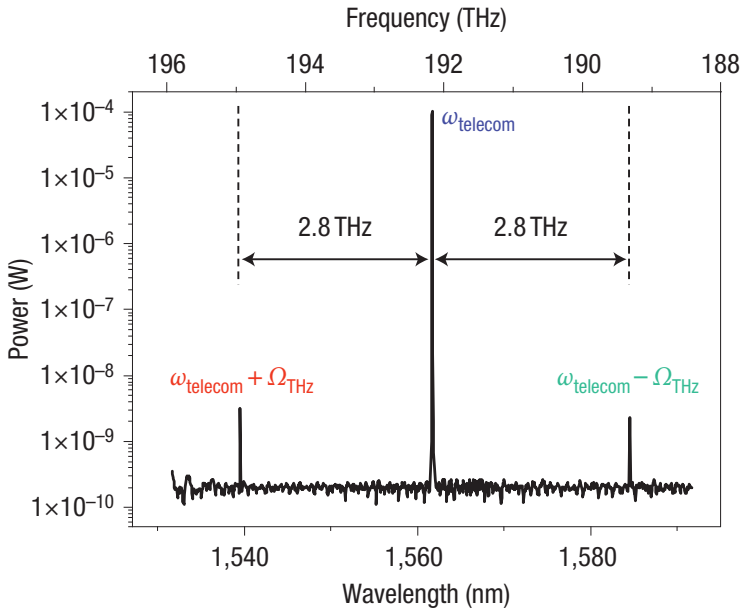

Figure 3.7: The output of the optical modulator using a terahertz quantum cascade laser. Figure is reprinted from [6].

part, we focus on the terahertz sources based on nonlinear interactions. Reported terahertz generation using a nonlinear process can be classified into three categories: terahertz generation in bulk crystals, periodically poled structures, and waveguide structures.

THz Generation in Bulk Crystals

Terahertz generation in bulk crystals has been shown in a variety of materials such as lithium niobate [54], GaSe [7, 55], $ZnGeP_2$, GaP [39]. Phase matching is provided using birefringence in the materials and angle tuning of the incident beams. In this kind of terahertz generation, lenses are used to focus the incident beams. The output powers are very low and the input powers should be very high. Therefore, pulsed laser inputs are used to prevent crystal damage.

For example an experimental setup for DFG-based terahertz generation using GaSe is depicted in figure 3.8 [7]. In this figure, M_1-M_7 are mirrors, A_1 and A_2 are attenuators, I_1 and I_2 are irises, WP_1, WP_2 are $\lambda/2$ plates, GP_1, GP_2 are Glan

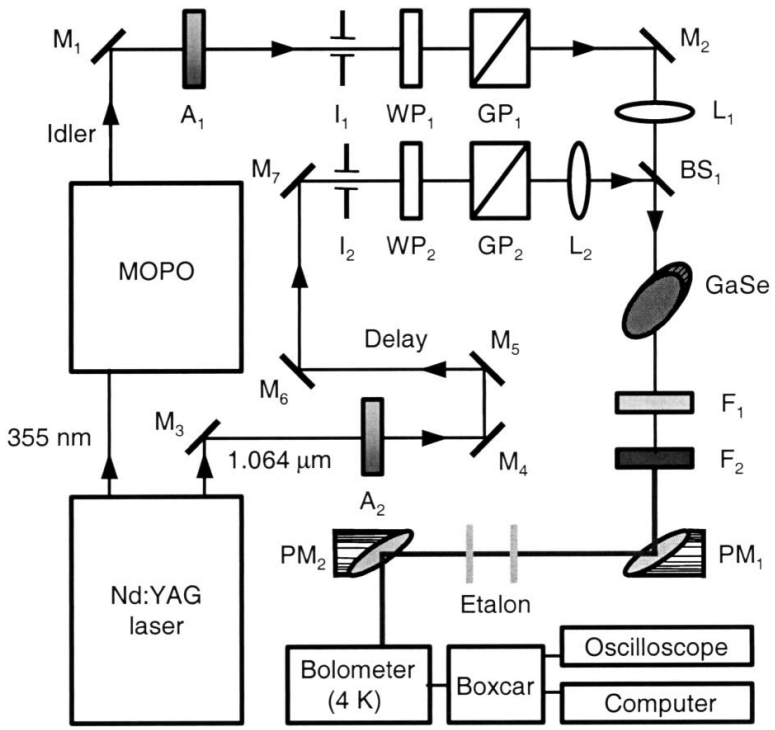

Figure 3.8: Experimental setup for DFG-based terahertz generation in GaSe. Figure is reprinted from [7].

polarizers, BS_1 is 50/50 beam splitter, L_1 and L_2 are convex lenses, PM_1 and PM_2 are parabolic mirrors, F_1 and F_2 are filters, and MOPO is master oscillator power oscillator. A Nd:YAG pulsed laser beam with duration of 10 ns, and repetition rate of 10 Hz is used as the pump power at 1.064 μm. For the second incident beam, the third harmonic of that laser is used at 355 nm as an input to a tunable optical parametric oscillator.

The terahertz radiation produced by this setup has a pulse duration of about 5 ns with a peak power of 69.4 W at 1.53 THz while the input pump has an energy of 6 mJ (average power of 600 KW). The generated pulse could have different applications, such as chemical sensing and differentiation of isotopic variants by measuring the rotational spectra of gases and terahertz imaging.

As well as the limitation on pulse duration of the generated signal in this method, the technique cannot be used in many materials. As discussed before, as a need for

birefringence phase matching, the crystal must be birefringent and transparent to the incident and generated wavelengths. Also, the experimental setup for terahertz generation in a bulk crystal, as depicted in figure 3.8 is complex and expensive.

THz Generation in Periodically Poled Structures

Periodically poled structures are used to provide phase matching for nonlinear mixing of optical wavelengths and can produce terahertz radiation. Lithium niobate [56], and GaAs [57, 8] are two crystals that have been used for this purpose. In this section we review the technique reported in [8].

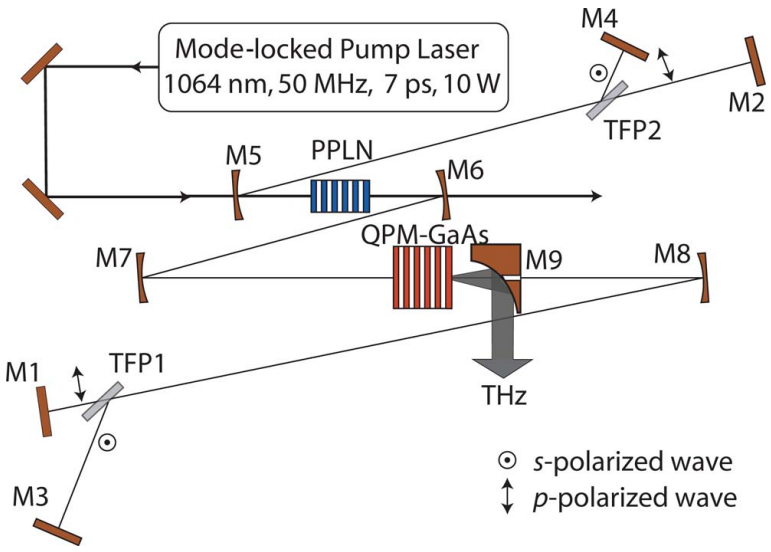

Figure 3.9: Experimental setup for DFG-based terahertz generation in quasi-phase-matched GaAs. Figure is reprinted from [8].

Figure 3.9 shows a schematic diagram of a system for DFG-based terahertz generation using quasi-phase-matched GaAs [8]. Similar to the example in previous section, a mode-locked Nd:YVO_4 laser at 1064 nm is used as the pump. The other wavelength is generated using an optical parametric oscillator based on a periodically poled lithium niobate (PPLN) device. The output power is enhanced using multiple cavities (mirrors M_1 - M_8) which are anti-reflection coated for the pump and high-reflection coated for other wavelengths.

The average output power reported in [8] reached 1 mW at 173 μm while the pump has a pulse energy of 2.3 μJ (average power of about 300 W).

Quasi-phase-matched terahertz generation requires pulsed high input powers. Moreover, the experimental setup for this technique, as depicted in figure 3.9 is complicated and expensive.

THz Generation in Waveguides

Terahertz generation in waveguide structures has been reported using the Raman nonlinear effect in rod-type GaP waveguides [58, 9].

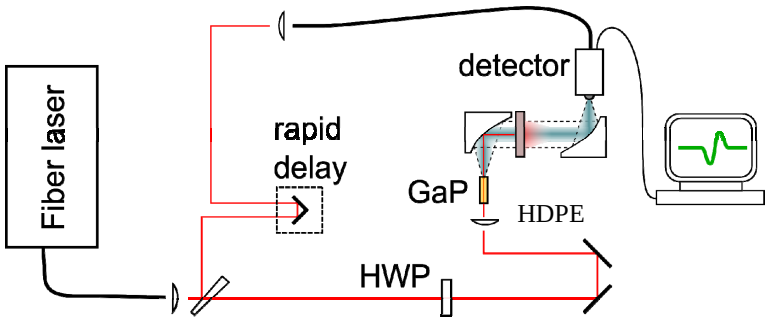

Figure 3.10: Experimental setup for terahertz generation in GaP rod-type waveguide. Figure is reprinted from [9].

Figure 4 illustrates the setup for terahertz generation in GaP [9]. A fiber laser is used to drive the system which is seeded by a passively mode-locked Nd:glass oscillator with an average power of 120 mW and a repetition rate of 72 MHz. The optical pulse has a duration of 110 fs and its spectrum is centered at 1.064 μm.

The improved efficiency of terahertz generation using the rod-type waveguide structure, which allows increasing the interaction length compared to a bulk crystal, is depicted in figure 3.11. With a 6-mm emitter, an average power of 120 μW is reported. It is also demonstrated that the dispersion can be tailored by changing the waveguide cross-section, therefore, other terahertz frequencies could be generated if other waveguide dimensions are used.

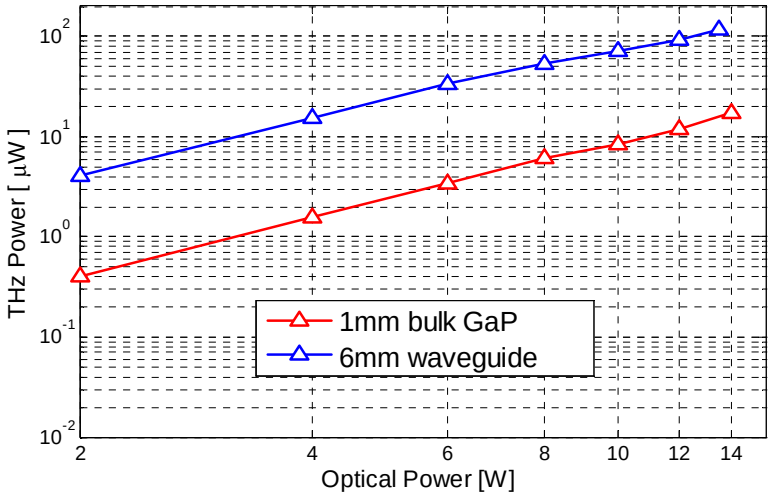

Figure 3.11: Comparison of terahertz output power versus optical input power using a GaP waveguide (upper line) and GaP bulk crystal (lower line). Figure is reprinted from [9].

3.6 Conclusion

At the beginning of this chapter we discussed waveguide structures, such as optical fibers and optical modulators, illustrating that modification of waveguide structures could enhance the nonlinear processes. We then reviewed some of the state-of-the art terahertz generation techniques using nonlinear effects. We observed that this kind of terahertz generation is limitted to pulsed terahertz generation, because the input optical powers should be very high, which damages the crystal in continuous form. Therefore, such high CW input powers cannot be achieved potentially. It is also shown in this chapter that experimental setups necessary for these forms of terahertz generation are complicated and expensive.

In this thesis, our approach to terahertz generation is based on waveguide structures. In the last example of this chapter it is shown that how a waveguide can increase the conversion efficiency. Moreover, we are interested in using tunable lasers, which are widely available for optical communication applications (1.5-1.6 μm). Using this type of lasers and optical amplifiers, the phase matching and output terahertz

frequency could be tuned by the input wavelengths.

Chapter 4

Design Background

4.1 Introduction

This chapter provides fundamental information for designing a device which can be used as a terahertz source by nonlinear mixing of optical wavelengths. The chapter is organized as following. In the first section material properties of GaAs and AlGaAs are reviewed. Material dispersion, nonlinear properties, and material absorption are the characteristics that have been discussed. In the second part some waveguides properties are reviewed and discussed.

4.2 Material Properties

4.2.1 Dispersive properties of GaAs

The dispersive properties of GaAs around the Reststrahlen's band (8-9THz) made the proposed designs feasible [35]. In this band the crystal shows strong coupling between photons and phonons associated with longitudinal optical and transverse optical lattice vibrations. This effect results in dispersion and absorption in the vicinity of the band. As a result, at the frequencies above this band, i.e. in the optical region, the dielectric constant is lower than the frequencies below the Reststrahlen's band, which is a key feature that makes the phase matching of optical and microwave waves possible. More details about the physics associated to this behavior could be

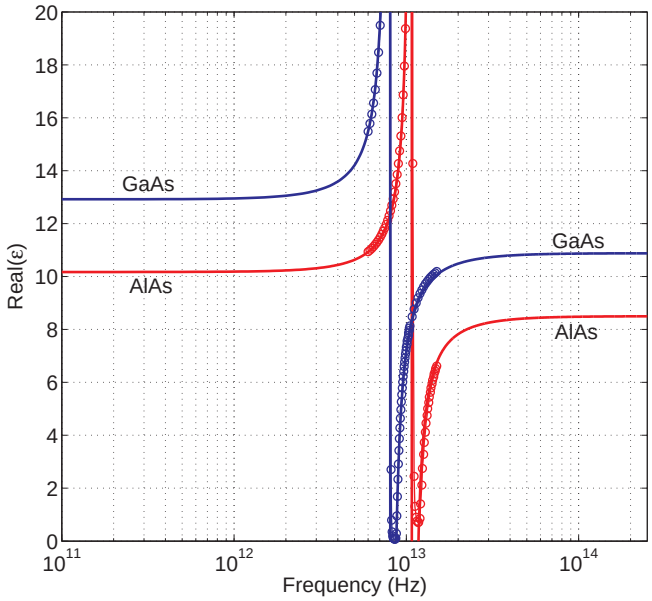

Figure 4.1: Dielectric constant of GaAs (blue) and AlAs (red) around Reststrahlen's band, measured values (circles) and approximated model (solid line).

found in many textbooks such as [59].

The dielectric constant of GaAs around its Reststrahlen's band could be obtained by:

$$\varepsilon(\omega) = \varepsilon(\infty)\left(1 + \frac{\omega_{LO}^2 - \omega_{TO}^2}{\omega_{TO}^2 - \omega^2 + j\omega\Gamma}\right), \tag{4.1}$$

where ω is the angular frequency, ω_{LO} and ω_{TO} are longitudinal and transverse optical phonon frequencies, and Γ is damping parameter ($\omega_{LO} = 36.21\ meV$, $\omega_{TO} = 33.23\ meV$, $\Gamma = 0.23\ meV$, and $\varepsilon(\infty) = 10.88$) [35]. Figure 4.1 shows the real part of the dielectric constant of GaAs around the Reststrahlen's band obtained from equation 4.1 and the measured values reported in [35].

For phase matching of a DFG process, as discussed in chapter 2, the group index of the optical signal should be matched to the phase index of the terahertz wave. For the material refractive index we have:

$$n(\omega) + jk(\omega) = \sqrt{\varepsilon(\omega)}, \tag{4.2}$$

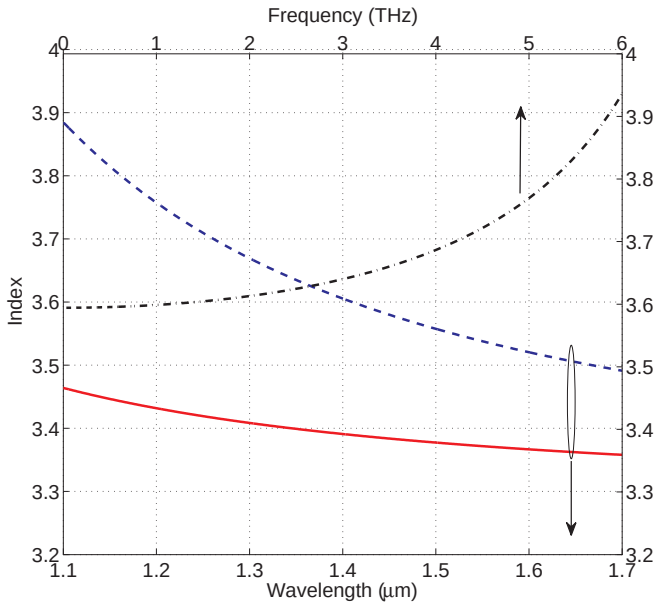

Figure 4.2: Refractive index of GaAs for terahertz range (black dash dot line), for optical range (red solid line), and optical group index (blue dash line).

where n is the real part of the refractive index, or the phase index, which determines the phase velocity of the wave in the material, and k is the imaginary part of refractive index which shows the amount of material absorption. To calculate the group index of the material, n_{gr}, we have:

$$n_{gr} = \frac{\omega dn}{d\omega}. \tag{4.3}$$

Figure 4.2 shows the refractive index and group index of GaAs over a range of optical wavelengths in comparison with the terahertz refractive index. At any frequency in the range of 0-6 THz, the terahertz refractive index can be matched to the group index of an optical wavelength between 1.1-1.4 μm. This means, for example, if we want to generate 2 THz, we have terahertz refractive index of 3.61, which should be equal to optical group index. That can be obtained at a central wavelength of 1.39 μm. By keeping the frequency difference of two incident optical wavelengths equal to 2 THz, they can be tuned to give the appropriate phase matching condition. Although the dispersive property of GaAs is promising for covering the

entire mentioned terahertz range, we also require precisely tunable laser sources and wideband high power optical amplifiers. Unfortunately, these cannot be found easily in that wide optical wavelength range. We prefer to operate near 1.55 μm where such components are widely available and inexpensive. However, in that range there is no corresponding terahertz frequency for phase matching. In the following chapter different waveguide structures are proposed to overcome this problem.

4.2.2 Dispersive properties of AlAs and AlGaAs

AlAs is another III-V compound which has a very similar dispersive properties, except that, due to the different atom sizes the vibrational states are different so the Reststrahlen's band is shifted as depicted in figure 4.1. The dielectric constant could be approximated by equation 4.1 with parameters: $\omega_{LO} = 48.6\ meV$, $\omega_{TO} = 44.43\ meV$, $\Gamma = 0.2\ meV$, $\varepsilon(\infty) = 8.5$ [60].

For $Al_xGa_{(1-x)}As$ compound, the dielectric constant could be accurately derived by [60]:

$$\varepsilon(Al_xGa_{(1-x)}As) = (1-x)\varepsilon(GaAs) + x\varepsilon(AlAs), \tag{4.4}$$

which is a linear interpolation of the dielectric constants of AlAs and GaAs according to x. Therefore, the dielectric constant of AlGaAs lies somewhere in between the curves in figure 4.1.

4.2.3 GaAs Absorption

The attenuation coefficient (α) for GaAs could be estimated using the complex form of dielectric constant obtained from equation 4.1.

$$\alpha = \omega\sqrt{\frac{\mu\varepsilon'}{2}}\left(\sqrt{1+\left(\frac{\varepsilon''}{\varepsilon'}\right)^2}-1\right)^{1/2}, \tag{4.5}$$

where ε' and ε'' are the real and imaginary parts of $\varepsilon(\omega)$, respectively.

Figure 4.3 shows the attenuation coefficient of AlAs and GaAs. As it can be seen,

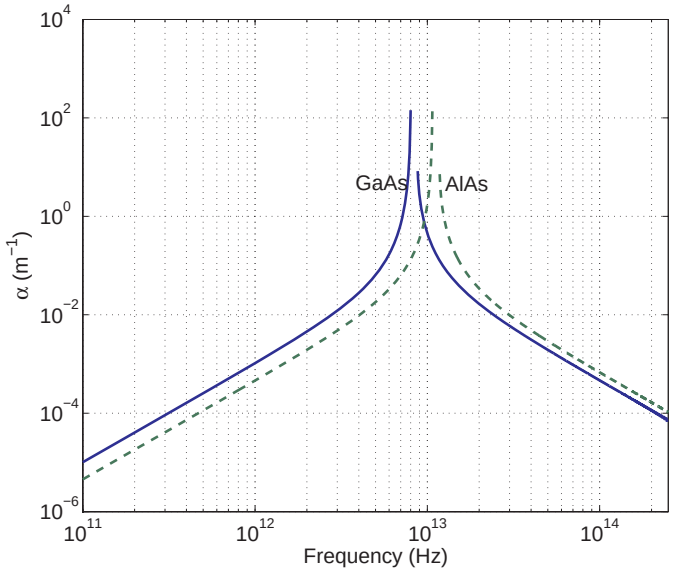

Figure 4.3: Attenuation coefficient in GaAs (blue solid) and AlAs (green dash).

Table 4.1: Second-order nonlinear susceptibilities for some crystals [1].

Material	$d(10^{-9} cm/statvolt)$
Quartz	$d_{11} = 0.96, d_{14} = 0.02$
$LiNbO_3$	$d_{22} = 7.4, d_{31} = 14, d_{33} = -98$
CdS	$d_{33} = 86, d_{31} = 90, d_{36} = 100$
GaAs	$d_{36} = 406$

in terahertz range this value is below 0.01 m^{-1} for up to 3THz.

4.2.4 Nonlinear Properties of GaAs

GaAs crystallizes as a zincblende structure [61] as depicted in figure 4.4. It possesses an unusually large second-order nonlinear susceptibility. Table 4.1 shows nonlinear susceptibilities of some crystals and GaAs. However, it doesn't have birefringence and therefore it cannot normally participate in phase-matched second-order processes [1]. The nonlinear susceptibility tensor for this crystal like other members of $\overline{4}3m$ group has the following situation: $d_{14} = d_{25} = d_{36} = d = \frac{1}{2}\chi^{(2)}$, while other components are zero.

Considering E_{x1}, E_{y1}, and E_{z1} are the components of the incident optical field at

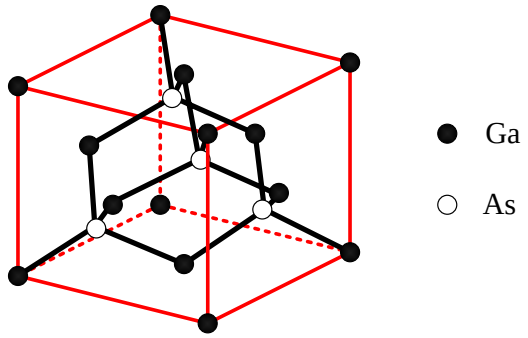

Figure 4.4: Illustration of a zincblende structure.

the highest frequency of ω_1 on the crystallographic axes (x, y, z) and E_{x2}, E_{y2}, and E_{z2} are those components at the other optical frequency of ω_2, for the total incident optical fields we have:

$$E_x = E_{x1}\cos(\omega_1 t + \phi_1) + E_{x2}\cos(\omega_2 t + \phi_2), \tag{4.6a}$$

$$E_y = E_{y1}\cos(\omega_1 t + \phi_1) + E_{y2}\cos(\omega_2 t + \phi_2), \tag{4.6b}$$

$$E_z = E_{z1}\cos(\omega_1 t + \phi_1) + E_{z2}\cos(\omega_2 t + \phi_2). \tag{4.6c}$$

Therefore, for the induced nonlinear polarization of the DFG process in GaAs at $\Omega_{THz} = \omega_1 - \omega_2$, according to equation 2.6, we have:

$$\vec{P}^{(DFG)} = \begin{pmatrix} P_x^{(DFG)} \\ P_y^{(DFG)} \\ P_z^{(DFG)} \end{pmatrix} = \frac{d}{2}\cos\left((\omega_1 - \omega_2)t + \phi_1 - \phi_2\right) \begin{pmatrix} E_{y1}E_{z2} + E_{y2}E_{z1} \\ E_{x1}E_{z2} + E_{x2}E_{z1} \\ E_{x1}E_{y2} + E_{x2}E_{y1} \end{pmatrix}. \tag{4.7}$$

Therefore,

$$\left|\vec{P}^{(DFG)}\right| = \frac{d}{2}\sqrt{\left(E_{y1}E_{z2} + E_{y2}E_{z1}\right)^2 + \left(E_{x1}E_{z2} + E_{x2}E_{z1}\right)^2 + \left(E_{x1}E_{y2} + E_{x2}E_{y1}\right)^2}. \tag{4.8}$$

To find the polarizations of the incident fields, i.e. the field components, at

which the magnitude of the induced polarization vector for DFG process is maximum, it is needed to maximize the right part of equation 4.8, which is not very easy. However, we consider the simple case of having both optical wavelengths with the same polarization and same magnitude of 1 ($\left|\vec{E}_{\omega_1}\right| = \left|\vec{E}_{\omega_2}\right| = 1$, $E_{x1} = E_{x2}$, $E_{y1} = E_{y2}$, and $E_{z1} = E_{z2}$).

Therefore, equation 4.8 becomes:

$$\left|\vec{P}^{(DFG)}\right| = d\sqrt{(E_{y1}E_{z1})^2 + (E_{x1}E_{z1})^2 + (E_{x1}E_{y1})^2}. \tag{4.9}$$

The maximum value of this function can be obtained numerically when $\vec{E}_{\omega_1}$, which has a magnitude of one, is represented in spherical coordinates. Figure 4.5 shows the values of the terms under the square route in the equation 4.9 versus ϕ and θ of the spherical coordinates. The maximum value on the curve, which is $\frac{1}{3}$, occurs at the equivalent point of $E_x = E_y = E_z = \frac{1}{\sqrt{3}}$. This means that the maximum magnitude of $\left|\vec{P}^{(DFG)}\right| = \frac{d}{\sqrt{3}}$ happens when the incident polarizations are parallel to the mentioned direction. It means the incident polarizations are parallel to $< 111 >$ direction of crystal, i.e. perpendicular to $< 111 >$ plane. Figure 4.6 shows the crystallographic axes of x, y, z and the physical crystal cut axes of x', y', z'. $\hat{z'}$ is the normal vector of $< 111 >$ plane in this crystal orientation [61].

As another example, in [58] the incident polarizations are orthogonal and parallel to the $< 110 >$ and $< 001 >$ directions, respectively. In this case, according to equation 4.8 the resulting nonlinear polarization vector would have a magnitude of $\frac{d}{2}$ considering incident magnitudes of one, which shows lower efficiency of the DFG process compared to previous case.

In this thesis it is assumed that all incident fields are parallel to $< 111 >$ direction of crystal. By this assumption, not only the nonlinear polarization would be maximum, but the generated field would also have the same polarization as the incident fields. This will prevent any polarization mismatch between the generated

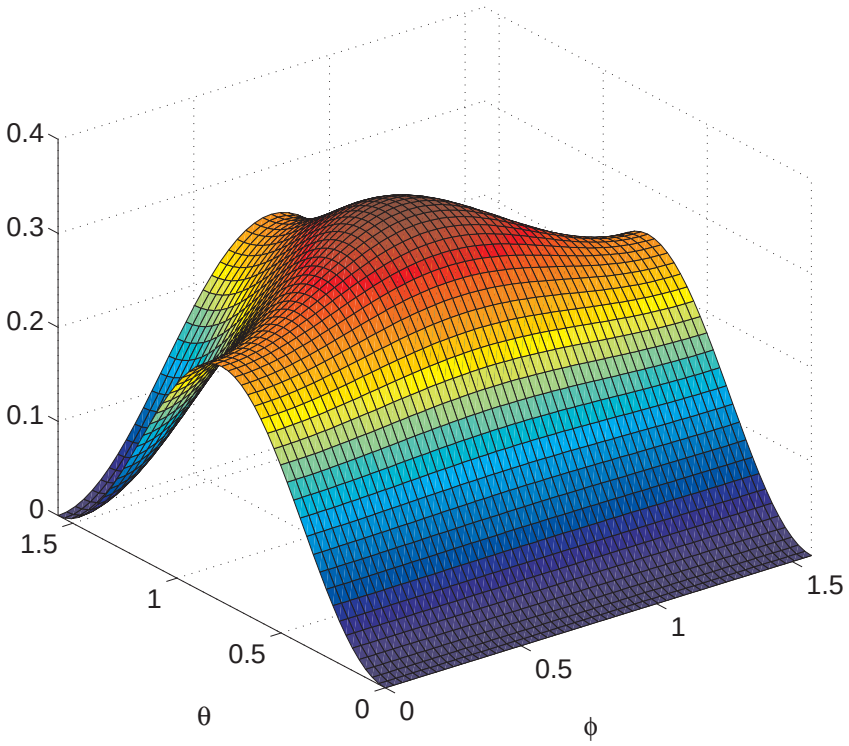

Figure 4.5: Values of the terms under square route in Equation 4.9 in spherical coordinates.

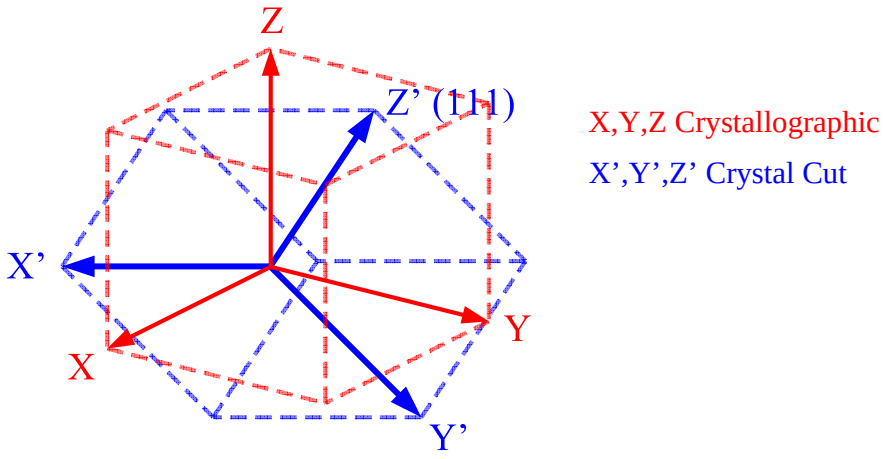

Figure 4.6: Illustration of $< 111 >$ crystal cut.

field and the waveguide mode. Using other incident linear polarizations may cause the generated polarization vector to be outside the incident polarization plane, which will appear as inefficient guiding.

4.3 Waveguide Design

Using waveguides for both terahertz and optical signals in this application is beneficial from several perspectives. First, we will be able to tailor the phase matching which is not achieveable in the bulk crystal of GaAs. We use waveguide phase matching in comparison to other phase matching techniques. On the other hand, using waveguides will let us extend the interaction length and consequently increase the efficiency of the terahertz generation. Also, it is easy to couple the generated terahertz wave to some other waveguides or antennas.

For the terahertz waveguiding two structures are employed in the studied devices in the next chapter. The first one is a parallel-plate waveguide which is a common microwave waveguide structure, and the other one is a metallic slit waveguide which is a relatively new waveguide for terahertz applications [62]. To study the behavior of the metallic slit waveguide, the slot line waveguide, as a well-known similar structure is studied in this section. For the optical wave-guiding the well-known dielectric slab structure is used. GaAs and AlGaAs are extensively used to build this kind of waveguide in many quantum-well-based structures such as diode lasers [63].

4.3.1 Terahertz Waveguides

There are many proposals for novel waveguides for terahertz applications published recently [64, 65]. However, we basically use the microwave concepts for our terahertz waveguides based on the facts that gold could be considered as a close-to-perfect electric conductor in the terahertz range [66] and the dielectrics that we will use, GaAs, AlGaAs, and silicon, have a very low absorption in this range.

In our application the terahertz waveguide is supposed to gather the generated

wave, and guide it as a single mode. The higher-order modes are not needed because their different phase velocities result in non-phase matched DFG processes which interfer with the phase matched process of the fundamental terahertz mode and decrease the efficiency.

Overview of all possible waveguides and study their properties is out of the scope of this thesis and there are many good references such as [46, 67]. In this part we review the properties of parallel-plate, slot line, and metallic slit waveguides. We use these waveguides because we are interested in TEM-like fundamental modes of these waveguides with low dispersive behavior.

Parallel-Plate Waveguide

The parallel-plate waveguide, depicted in figure 4.7, is of particular interest because it supports a non-dispersive TEM mode. The TE and TM modes of this kind of waveguide is similar to TE and TM modes of a rectangular waveguide which have cut-off frequencies and are very dispersive close to the cut-off frequency. Details about the behavior of these modes could be found in [68].

For the TM_n mode of a infinitely wide parallel-plate waveguide the field components are:

$$H_y = \frac{j\omega\epsilon}{k_c} A_n \cos\frac{n\pi x}{d} e^{-j\beta z}, \tag{4.10a}$$

$$E_x = \frac{-j\beta}{k_c} A_n \cos\frac{n\pi x}{d} e^{-j\beta z}, \tag{4.10b}$$

$$E_y = H_x = 0, \tag{4.10c}$$

where k_c is the cutoff wave number, and β is the propagation constant. For $n = 0$ the TM_n mode turns into the TEM mode electric field is in the y direction and magnetic field is in x. The simulated electric field vectors for a real parallel-plate waveguide is depicted in figure 4.8, showing the fringing fields around the corners.

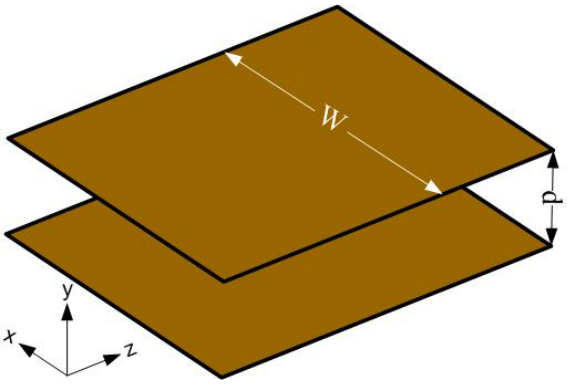

Figure 4.7: A parallel-plate waveguide.

(a) (b)

Figure 4.8: Electric field distribution of the TEM mode of a parallel-plate waveguide, (a) Field vectors (b) Field magnitude.

For the TE_n mode of an infinitely wide waveguide we have:

$$E_y = \frac{j\omega\mu}{k_c} B_n \sin\frac{n\pi x}{d} e^{-j\beta z}, \tag{4.11a}$$

$$H_x = \frac{j\beta}{k_c} B_n \sin\frac{n\pi x}{d} e^{-j\beta z}, and \tag{4.11b}$$

$$H_y = E_x = 0. \tag{4.11c}$$

From the polarization perspective there is no overlap between TE modes and the TEM mode. However, the vertical polarization not only could be coupled to the TEM mode but also could it be coupled to the TM modes. Therefore the higher-order TM modes are important in this case. When the area between two conductors are filled with a dielectric, which is the case in our designs, the TEM mode will turn into a quasi-TEM mode, which has a frequency dependent behavior as will be shown in the next chapter.

Slot Line Waveguide

Slot line usually consists of a narrow gap in a conductive coating on one side of a dielectric substrate as depicted in figure 4.9. If the substrate permittivity is sufficiently high, the slot mode wavelength will be much smaller than free space wavelength, and the fields will be closely confined near the slot. However, unlike microstrip and coplanar lines, the TEM or quasi-TEM mode doesn't propagate. It could be explained due to the fact that, the infinite extent of the metallic layers in y direction doesn't let the magnetic field lines to be closed in xy plane to form a TEM mode. Therefore, as depicted in figure 4.9, magnetic field will have a component in the direction of propagation (z). This behavior of the field will result in the TE-like nature of the slot mode. On the other hand, because of the extension of the electric field in the dielectric and air, it will also have a component in the direction of propagation. Therefore, the slot mode is known as a quasi-TE mode, which has all six components of electric and magnetic fields and can propagate in the frequency range of: $0 < f < \infty$ [69].

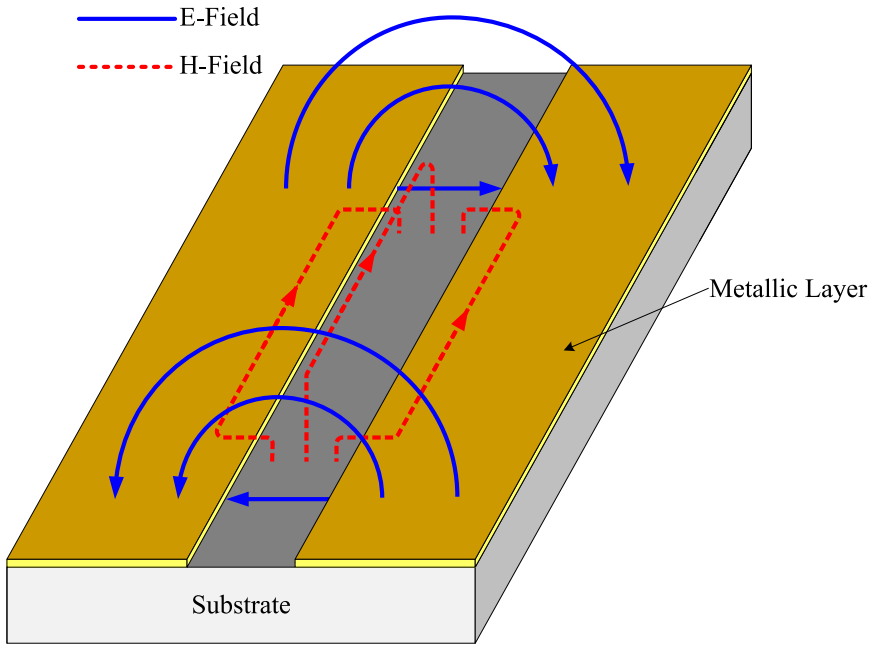

Figure 4.9: A slot line waveguide.

To study the behavior of this mode in such a waveguide, simulations are performed for two cases, one is with different dielectrics on each side and the other is using a uniform dielectric. Both simulations are done for an extremely thin metallic layer at the wavelength of ten times the slot width. For the first case the maximum value of magnetic field in the direction of propagation is 5 orders of magnitude smaller than the maximum value of magnetic field in x, and for the second case it is 6 orders of magnitude smaller. These results show that although the nature of this mode is TE but its behavior is very similar to a TEM mode especially for a unique dielectric. It can also be concluded that the dispersive behavior of the slot mode in waveguides with a substrate results from the frequency dependent distribution of the fields in different dielectrics. The field distribution for the second case is shown in figure 4.10. More details about the behavior of this kind of waveguide can be found in [69, 70].

Metallic Slit Waveguide

Metallic slit waveguide, which is depicted in figure 4.11, is a new type of waveguide recently proposed for terahertz applications [62]. Simply speaking, this waveguide is

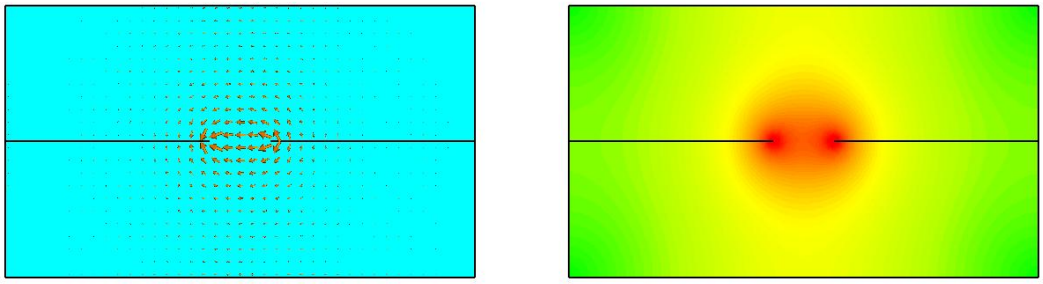

(a) (b)

Figure 4.10: Electric field distribution of the slot mode of a slot line waveguide in a uniform dielectric, (a) Field vectors (b) Field magnitude.

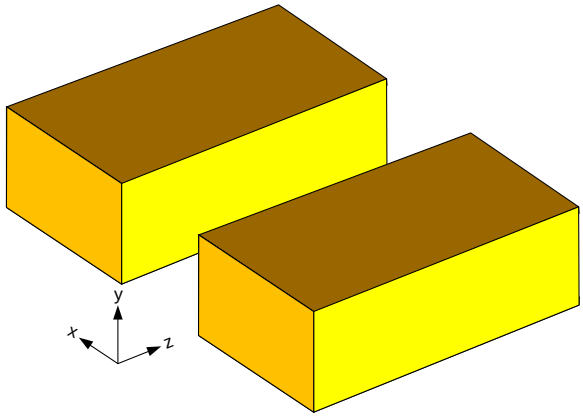

Figure 4.11: A metallic slit waveguide.

the same as a slot line with a uniform dielectric where the thikness of the conductors are increased and is comparable to the slot width. The fundamental mode of this waveguide, which is named TEM mode in [62], is not naturally a TEM mode and is very similar to the slot mode discussed earlier. The main difference is that the thicknesses of the metallic walls increase the field concentration in the slit area drastically. This cause that the components of fields in the direction of propagation decrease significantly and the mode behaves as an almost non-dispersive frequency independent mode. Because of this behavior we will name this mode the TEM-like slit mode.

Field distribution of the fundamental mode of this waveguide is depicted in figure 4.12. Compared to the slot line waveguide discussed in previous section, the field components in the direction of propagation are much smaller than the transverse field components due to the increase of the confinement of the mode in the slit area.

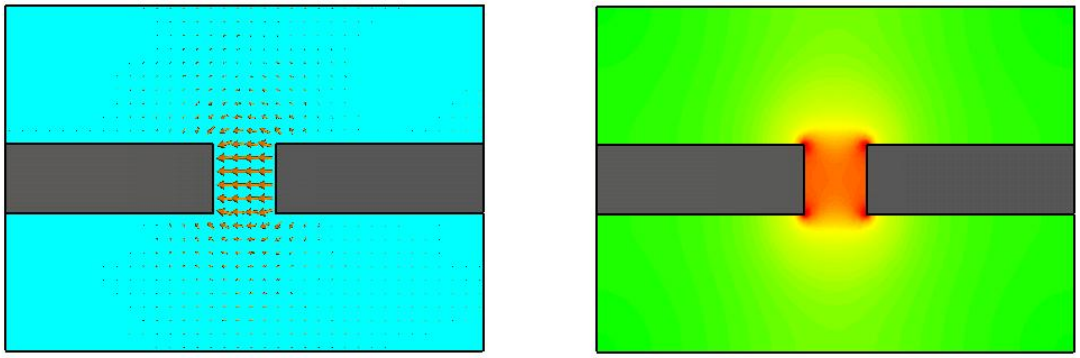

(a) (b)

Figure 4.12: Electric field distribution of the fundamental mode of a metallic slit waveguide in a uniform dielectric, (a) Field vectors (b) Field magnitude.

The loss of this mode has been measured to be less than 0.04 $\frac{db}{mm}$ for up to 1 THz in [62].

4.3.2 Optical Dielectric Slab Waveguide

Dielectric slab waveguides are well-known structures in optics. A schematic diagram of a symmetric dielectric slab waveguide is depicted in figure 4.13. For the TE modes of this waveguide where just E_y,H_x, and H_z exist, the Maxwell's equations will be reduced to:

$$E_y = -\frac{\omega\mu}{\beta}H_x, \tag{4.12a}$$

$$\frac{\partial E_y}{\partial x} = -j\omega\mu H_z. \tag{4.12b}$$

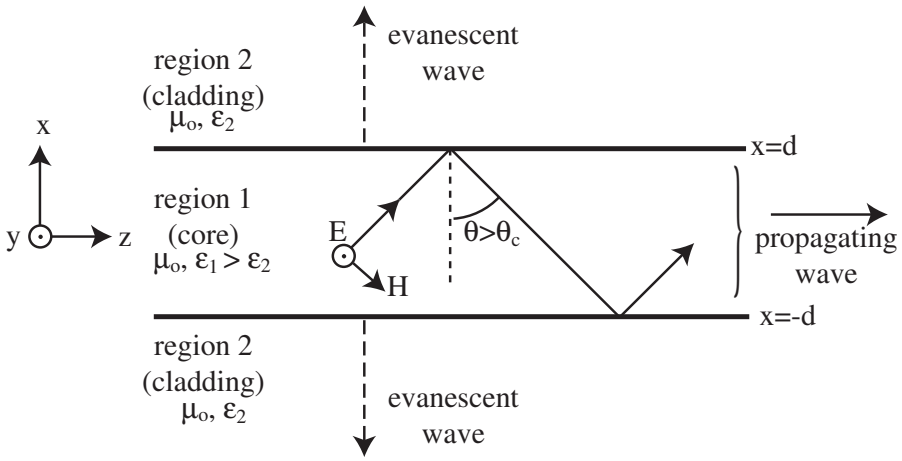

Figure 4.13: A symmetric dielectric slab waveguide.

For the TM modes involving H_y,E_x, and E_z, they would be:

$$H_y = -\frac{\omega\varepsilon}{\beta}E_x, \tag{4.13a}$$

$$E_z = -\frac{j}{\omega\varepsilon}\frac{\partial H_y}{\partial x}. \tag{4.13b}$$

The solutions for the TE modes could be separated as odd ($E_y(x,z,t) = E_y(-x,z,t)$) and even ($E_y(x,z,t) = -E_y(-x,z,t)$) modes. For the even TE modes the electric field is:

$$E_y = A\exp\left(-p\left(|x|-d\right)-j\beta z\right) \quad |x| \geq d, \tag{4.14a}$$

$$E_y = B\cos(hx)\exp(-j\beta z) \quad |x| \leq d, \tag{4.14b}$$

and for the odd TE modes we have:

$$E_y = A\exp\left(-p\left(|x|-d\right)-j\beta z\right) \quad x \geq d, \tag{4.15a}$$

$$E_y = -A\exp\left(p\left(|x|-d\right)-j\beta z\right) \quad x \leq d, \tag{4.15b}$$

$$E_y = B\sin(hx)\exp(-j\beta z) \quad |x| \leq d, \tag{4.15c}$$

where p and h are positive numbers, and β is the propagation constant of the mode. Applying the continuity condition for the even modes results in:

$$pd = hd\tan(hd), \tag{4.16}$$

and for the odd mode results in:

$$pd = -hd\cot(hd). \tag{4.17}$$

On the other hand, the wave equation in the core region is:

$$\frac{\partial^2}{\partial x^2}E(x,y) + \left(k_0^2 n_1^2 - \beta^2\right)E(x,y) = 0, \tag{4.18}$$

and in the cladding region is:

$$\frac{\partial^2}{\partial x^2}E(x,y) + \left(k_0^2 n_2^2 - \beta^2\right)E(x,y) = 0, \tag{4.19}$$

where, $k_0 = \frac{\omega}{c}$, and n_1, n_2 are the refractive index of core and cladding, respectively. Substituting the field solutions of the modes into these equations, gives:

$$h = \sqrt{n_1^2 k_0^2 - \beta^2}, \tag{4.20}$$

$$p = \sqrt{\beta^2 - n_2^2 k_0^2}. \tag{4.21}$$

By substituting these two equations into equations 4.16, and 4.17, and changing the "cot" to"tan", and using effective index of each mode (n_{eff}) instead of $\beta = k_0 n_{eff}$ an equation for both even and odd TE modes is obtained, which is:

$$\frac{k_0 d}{2}\sqrt{n_1^2 - n_{eff}^2} = \tan^{-1}\sqrt{\frac{n_{eff}^2 - n_2^2}{n_1^2 - n_{eff}^2}} + (m-1)\frac{\pi}{2}, \tag{4.22}$$

where m= 1, 2, 3, ... is the index of the TE modes. For the bounded modes, where the field distrubution decays exponentially in the cladding, the square routes should return real values. It means: $n_2 < n_{eff} < n_1$. Equation 4.22 always has a bounded solution for m=1, which means the fundamental TE mode of the dielectric slab waveguide does not have a cut-off frequency. The existence of higher order modes depends on d, n_1, and n_2.

For TM modes, similar calculations result in:

$$\frac{k_0 d}{2}\sqrt{n_1^2 - n_{eff}^2} = \tan^{-1}\left(\frac{n_1}{n_2}\sqrt{\frac{n_{eff}^2 - n_2^2}{n_1^2 - n_{eff}^2}}\right) + (m-1)\frac{\pi}{2}. \tag{4.23}$$

Details about numerical calculation of these equations to find the supporting modes and their effective indices in a symmetric slab waveguide is discussed in appendix A. Figure 4.14 shows the fundamental TE and TM modes of a dielectric slab waveguide which are tightly confined in the core region.

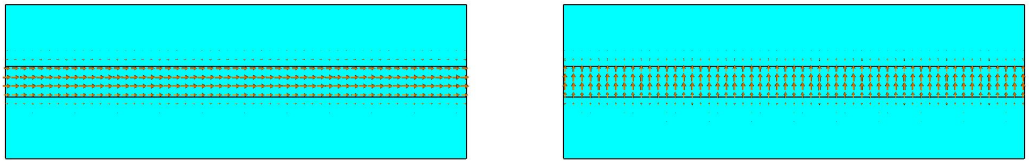

(a) (b)

Figure 4.14: Electric field distribution of the fundamental TE and TM modes of a dielectric slab waveguide on xy plane (a) TE (b) TM.

4.4 Conclusion

In this chapter we reviewed some fundamental material properties of GaAs and AlGaAs which are used as the main crystal for difference frequency mixing for terahertz generation in this thesis. Moreover, we studied the waveguide properties of the structures used in our proposed devices in the next chapter. The waveguide structures presented in the next chapter as terahertz sources are the combination of the struc-

tures and materials discussed in this chapter.

Chapter 5

Device Design

5.1 Introduction

In this chapter three devices are proposed to be used for generating terahertz radiation by mixing two appropriate optical wavelengths using GaAs or AlGaAs crystal. GaAs is of particular interest because not only does it have a very high second-order nonlinear coefficient, an order of magnitude higher than similar compounds such as $LiNbO_3$, but also the terahertz absorption is relatively low in this crystal. The challenging part is providing phase matching for the crystal. Because of the non-birefringent properties of this crystal, birefringence phase matching is not feasible and quasi-phase matching is hard to achieve due to the complicated process of ordering the nonlinear susceptibility in semiconductors. We are interested in combining appropriate optical and terahertz waveguides to provide phase matching for down conversion of optical wavelengths. The device is aimed to phase-match the DFG-based terahertz generation process for the optical wavelengths in the range of 1.5-1.6 μm where tunable lasers and high power amplifiers are available for telecommunication applications.

The design objective is matching the group index of the optical waveguide in the range of 1.5-1.6 μm to the effective index of the terahertz waveguide for a wide range of terahertz frequencies. Such a device can be used as a tunable continuous-wave coherent source of terahertz radiation by applying appropriate optical wavelengths.

Output terahertz frequency is equal to the difference-frequency of the incident wavelengths, and by changing the central wavelength of the incident wavelengths which their difference frequency is locked, the phase matching condition can be obtained.

Three waveguide structures are proposed and studied for DFG-based terahertz generation. The first structure is previously used as a terahertz quantum cascade laser [71] and also for modulation of an optical beam with a terahertz signal [6]. Here we study it as a terahertz source. The next two devices are novel structures proposed for phase-matching terahertz and optical waves: A metallic slit waveguide filled with GaAs and sandwiched between silicon layers, and a combination of a metallic slit waveguide and a dielectric slab waveguide with GaAs and AlGaAs. The first device, which is easy to build, has not acceptable terahertz generation performance, however, it can be used as a terahertz detector with satisfactory performance. The second one has a great terahertz generation performance and could be used in many applications where such phase matching of terahertz and optical waves are necessary.

5.2 Device I

Combination of Parallel-Plate and Dielectric Slab

The combination of a parallel-plate waveguide for the millimeter-wave and a dielectric slab waveguide for the optical signal is a structure that has been used for applications where wave-guiding for both ranges of frequencies is needed, such as terahertz quantum cascade lasers [71] and optical beam modulation of terahertz signals [6].

The modulation of the optical beam is obtained based on two processes of sum and difference frequency generations resulting in two optical sidebands. As it is shown in [6] the phase matching for these processes could be obtained for a narrow range of frequencies which depends on the dimensions of the structure.

In this section we study this type of device depicted in figure 5.1 as a source of terahertz radiation by difference frequency mixing. We evaluate the behavior of this

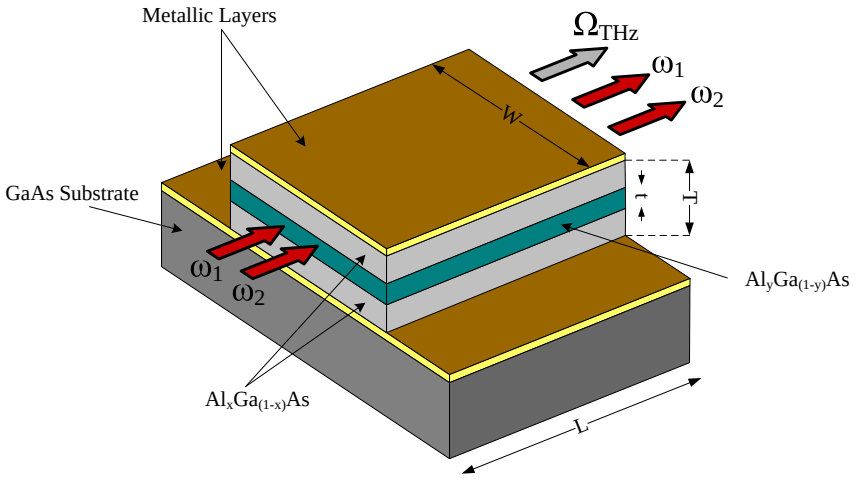

Figure 5.1: Combination of a parallel-plate and a dielectric slab waveguides for THz generation

structure and we will verify our simulation results by some of the measured values in [6].

Figure 5.1 shows the structure which is a dielectric slab waveguide for optical signal sandwiched between two metallic layers as a terahertz waveguide. The terahertz waveguide is similar to a microstrip waveguide in which the dielectric only exists underneath the top metallic layer rather than being infinitely wide. The fundamental vertically polarized optical mode and terahertz quasi-TEM mode of the structure which are the desired modes to allow the nonlinear process are depicted in figure 5.2. The field distribution for the terahertz quasi-TEM mode is very similar to a parallel-plate waveguide because the bottom metallic layer acts as a symmetry plane for the quasi-TEM field. Moreover, there is less fringing fields than a parallel-plate waveguide because of the existence of the dielectric. For the optical waveguide, in the horizontal direction of the waveguide there is a symmetric slab waveguide, in which the optical mode exponentially decays toward the metallic layer, and for the vertical direction, there is a a combination of air-dielectric-air, which makes another symmetric slab waveguide.

The main concern about this structure is that the optical waveguide supports sev-

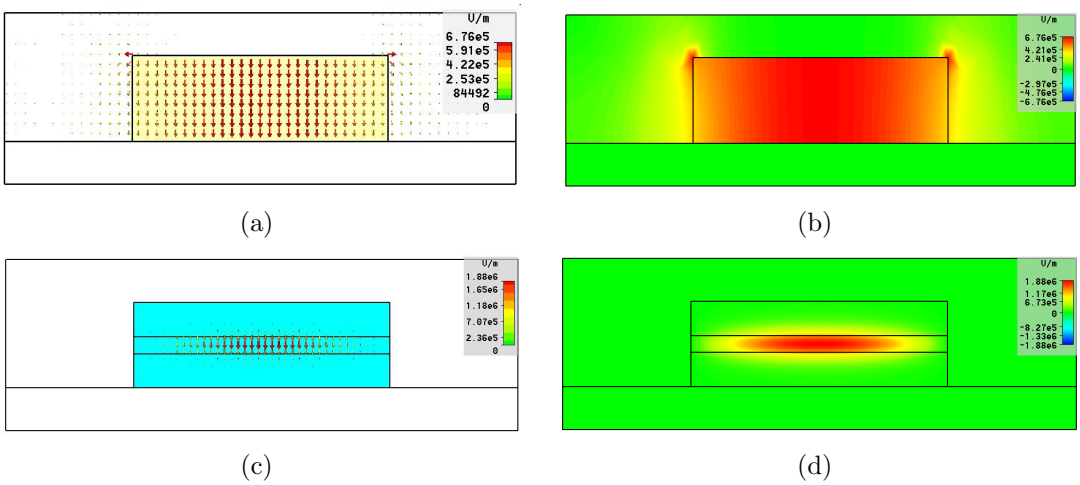

Figure 5.2: Electric field distribution of the fundamental modes in parallel-plate structure. (a) Field vectors at 2THz, (b) Field magnitude at 2THz, (c) Field vectors at 1.55μm, (d) Field Magnitude at 1.55μm.

eral modes. The combination of air-dielectric-air in the horizontal direction, provides a multimode waveguide for optical beam, where the thickness of the guiding layer is much larger than the wavelength and the index step is relatively high (more than 3). Therefore, for the vertically polarized optical wavelengths there would be thousands of guiding modes. This means, practically, even if the fundamental mode of interest is excited there would be some residual excitation and propagation of other modes. However, there are two factors that make those residually excited higher-order modes unimportant. The first point is the second-order nature of difference frequency generation. As it could be seen in equation 2.34, the generated terahertz amplitude is proportional to the square of the optical amplitude. Considering that the next excited higher-order mode has an amplitude of 0.1 of the main mode, the resulted terahertz amplitude which is not phase-matched with the main generated one would be 0.01 of the main generated terahertz field considering the same overlap factor. The second fact that makes the role of higher order modes insignificant is the lower overlap factor for higher-order modes than the lower-order modes. Considering equation 2.33, the overlap coefficient for higher-order optical modes is much lower

than the overlap between the fundamental terahertz and optical modes which results in a much lower amplitude terahertz generation by those residual modes.

As it was expected from the phase-matching criteria for modulation reported in [6], the device could not work in a wide range of terahertz frequencies. This fact also has been shown in our criteria depicted in figure 5.3. Terahertz effective index of the waveguides for two different thiknesses and widths are compared to the optical group index. For the AlGaAs in the guiding optical layer of the dielectric slab waveguide, y=0.184, and for the claddings, x=0.18. In this plot there is only one curve for the optical group index for all dimensions because the effective index and consequently the group index of the fundamental mode does not change much by the dimension of a multimode slab waveguide. The difference is less than 0.1% calculated using effective index method discussed in appendix A.

Figure 5.3 shows that, due to very dispersive behavior of the terahertz mode, which is the result of material dispersion combined with waveguide dispersion, optical wavelengths in the range of 1.5 - 1.6 μm can be matched to a very narrow range of terahertz frequencies, couple of hundreds of megahertz in the best cases. The material dispersion of GaAs is discussed in previous chapter and the waveguide dispersion is resulted from the combination of air dielectric. This combination changes the frequency independent field distribution of the TEM mode to a frequency dependent quasi-TEM mode where for higher frequency the field is more confined in the dielectric. As a result, for higher frequencies the effective index is closer to the GaAs refractive index. If a single frequency or a narrowband terahertz source is needed this structure will be a good choice, because by varying the dimensions phase matching could be obtained from almost zero to about 4THz.

The overlap between the terahertz and optical modes for a device with $w = 30\mu m$ and $T = 10\mu m$ at 2.5 THz and 1.55 μm is about 0.3. It means that if the incident wavelengths around 1.55 μm have the difference frequency of 2.5THz and each one

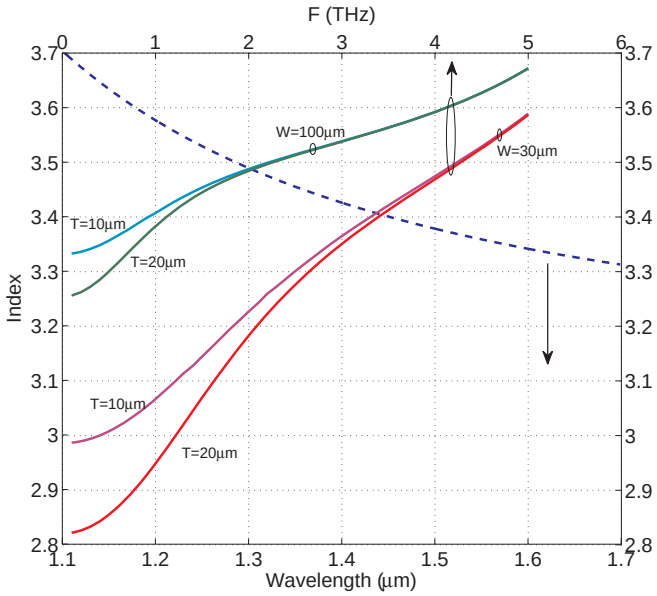

Figure 5.3: Terahertz effective index in comparison to the optical group index of the Parallel-Plate structure for different dimensions.

has a power of 500mW, the output terahertz power for phase matched condition and device length of L=4 cm would be 0.2 mW according to equation 2.34.

Different fabrication techniques have been used to realize such a structure for previous applications [6, 71]. Molecular Beam Epitacy (MBE) has been used for crystal growth, which is necessary to engineer the superlattice structure required for quantum cascade lasing. For the metallic layers several different approaches have been employed. Deposition of gold layers and using flip-chip [71] is one of the approaches. The other very common method is using highly doped layers as a conductor for terahertz frequencies [72]. The main disadvantage of this technique is the relatively high loss associated with the doped region.

The combination of a parallel-plate and a slab waveguide which has been used as a quantum cascade lasers and for optical beam modulation of a terahertz signal has been proposed and studied for terahertz generation by nonlinear difference-frequency mixing. The phase matching, as was expected from [6], cannot be achieved for a wide terahertz range due to the dispersive behavior of the fundamental terahertz mode.

However, the overlap of the optical and terahertz modes are reasonably high and the output terahertz power could be relatively high. Therefore, this device, which has been build for other applications, can be used for narrow-band terahertz generation by DFG.

5.3 Device II

Metallic Slit Waveguide of GaAs/Silicon

In this section we propose a novel waveguide structure for phase-matching the DFG process for terahertz generation. Figure 5.4 shows the proposed device which is a metallic slit waveguide [62] with GaAs in the slit area sandwiched between two layers of silicon. In this structure a metallic slit waveguide is used for terahertz wave and there is no waveguide for optical signal. Therefore, Gaussian beam propagation is assumed for the optical signal which restricts the device length according to the aperture size.

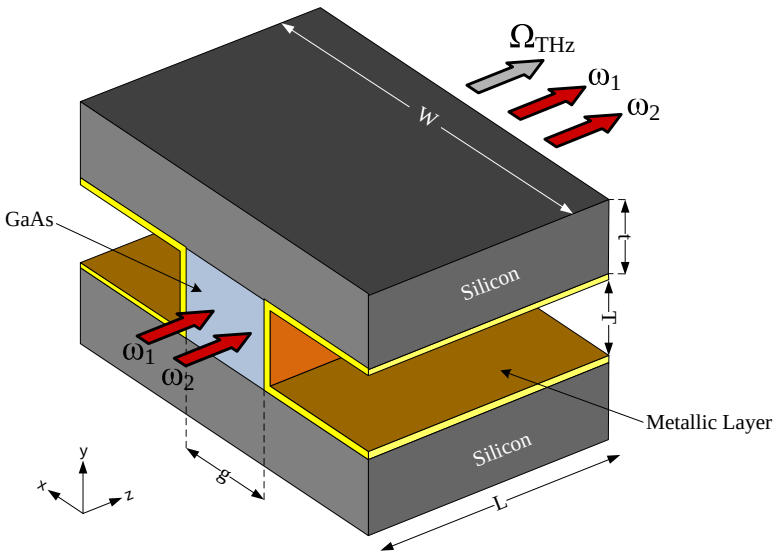

Figure 5.4: Metallic slit waveguide filled with GaAs and sandwiched between silicon layers.

For the optical beam, the field is supposed to be far enough from the metallic layers to prevent any reflection and extension of optical field into conductors. Therefore,

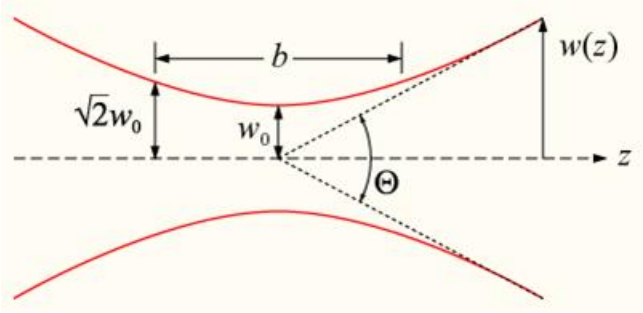

Figure 5.5: Gaussian beam propagation.

according to Gaussian beam propagation [73], which is depicted in figure 5.5, we have:

$$b = 2z_0 = \frac{2\pi w_0^2}{\lambda}. \tag{5.1}$$

It means that the device length depends on the aperture size (ω_0), the larger the aperture, the longer the device. On the other hand, for the terahertz waveguide, increasing the gap size will result in appearance of higher-order TM modes which are not suitable for this application. As discussed in previous chapter, due to the polarization mismatch between the TE and TEM modes of the parallel-plate waveguide, only TM higher-order modes are important. So, we will restrict our aperture dimension to operate below the cut-off of the first parallel-plate TM mode. The cut-off frequency of TM_n is:

$$f_c = \frac{n}{2g\sqrt{\mu\varepsilon}}. \tag{5.2}$$

Based on this equation for $g = 25\mu m$ the cut-off of the first TM mode is around 2THz, which means the TM higher order modes could not propagate at frequencies below 2THz. T is also equal to 25 μm. Therefore, based on equation 5.1 the maximum length of the device would be about 634 μm. This length is very short for the nonlinear interactions.

Figure 5.6 shows the field distribution of the terahertz mode. The terahertz mode is the fundamental TEM-like mode of the slit structure which is mainly inside the

(a) (b)

Figure 5.6: Electric field distribution of the terahertz mode of in metallic slit - silicon structure. (a) Field vectors at 2THz, (b) Field magnitude at 2THz.

GaAs layer and extends to silicon outside the gap. This field extension, which is more for lower terahertz frequencies, will results in compensation of the index mismatch at the terahertz range and optical range of interest. As depicted in figure 5.7, compared to figure 4.2 the terahertz effective index is reduced due to the extension of the terahertz mode into silicon, which has a relatively non-dispersive dielectric constant of $\simeq 11.9$ in the desired range and has very low terahertz absorption [66]. It shows that phase matching is obtained in the range of 0-1.7 THz and optical wavelengths in the range of 1.5-1.6 μm.

According to equation 2.34, for terahertz generation, when the input pumps have power of 1 W each, the output power at 1THz is about 0.03 μW which is not an impressive value. However, this device could be used as an optical modulator for terahertz detection while the DFG process generates an optical side band. For this application, a 5 mW terahertz wave at the input of the waveguide, and a pump power of 1W at 1.55 μm, results in output power of the optical sideband of about 2.5 μW. This could be detectable by a large margin using a photo detector. Increasing the aperture size for this application is possible because the incident terahertz wave can be carefully coupled only to the fundamental mode. While potentially useful, output power is limited for both terahertz generation and detection or modulation by the short interaction length and large aperture of device, which decreases the incident electric field strength. To benefit from the widely tunable phase matching scheme

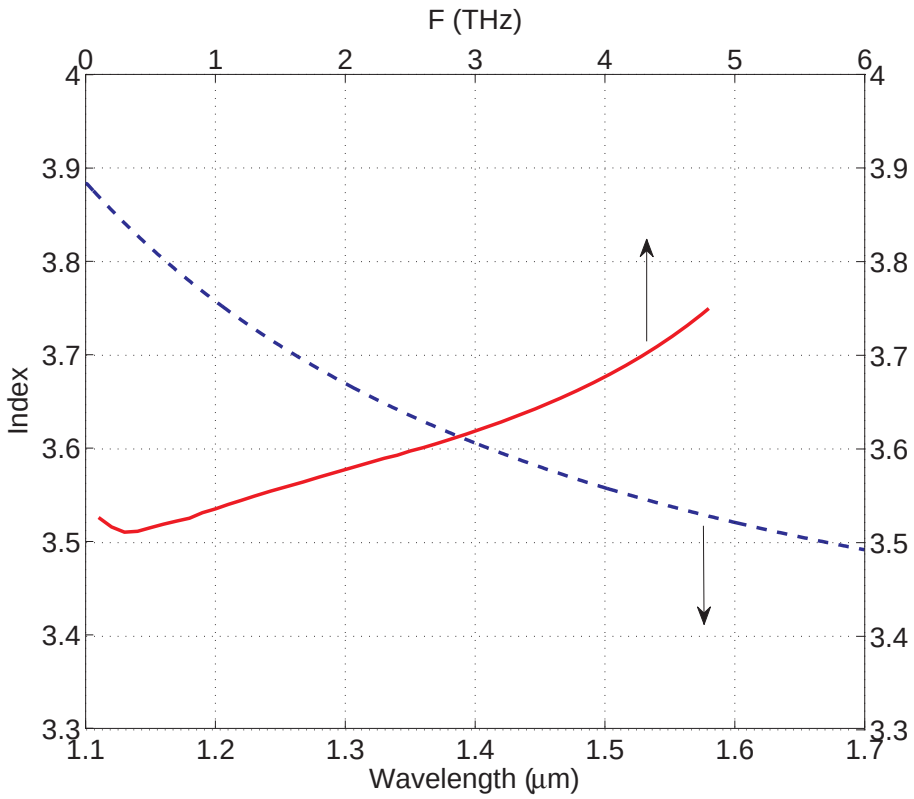

Figure 5.7: Terahertz effective index in comparison to the optical group index of the slit - silicon structure.

and generate higher output powers, device length could be extended significantly by integrating an appropriate optical waveguide which is the basic idea of the next proposed device.

Due to the large dimensions of the device in comparison to the state-of-the-art fabricated devices, the combination of the GaAs crystal and metallic slit without the cladding may be compatible with bulk fabrication techniques. While novel and potentially challenging, an outer cladding material of silicon might be applied using techniques such as flip-chip solder bonding [74].

5.4 Device III

Combination of Metallic Slit and Dielectric Slab

The last structure, which has an outstanding performance in comparison to the previously discussed devices, is a combination of a metallic slit waveguide and a ridged slab waveguide. This structure works single mode for both terahertz and optical signals, and provides higher bandwidth, overlap, and interaction length for the nonlinear process. The aperture size is significantly decreased which results in higher field strengths and therefore higher conversion efficiency. Moreover, wave-guiding both terahertz and optical signals let us extend the length of the device up to couple of centimeters and consequently increase the conversion efficiency.

The proposed device is an integration of a three layer ridge slab waveguide, for optical signal, with a metallic slit waveguide for terahertz wave, as depicted in figure 5.8. The dimensions of the waveguides are depicted in the figure. The optical waveguide supports only a single mode for wavelengths longer than 1.45 μm and has a mode distribution as depicted in figure 5.9. For the terahertz wave, the metallic slit waveguide is used because it supports a non-dispersive TEM-like mode and the field is tightly confined in the slit area, as depicted in figure 5.9. The outer area of the slit waveguide is filled with $Al_zGa_{(1-z)}As$, z=0.4 to obtain appropriate terahertz

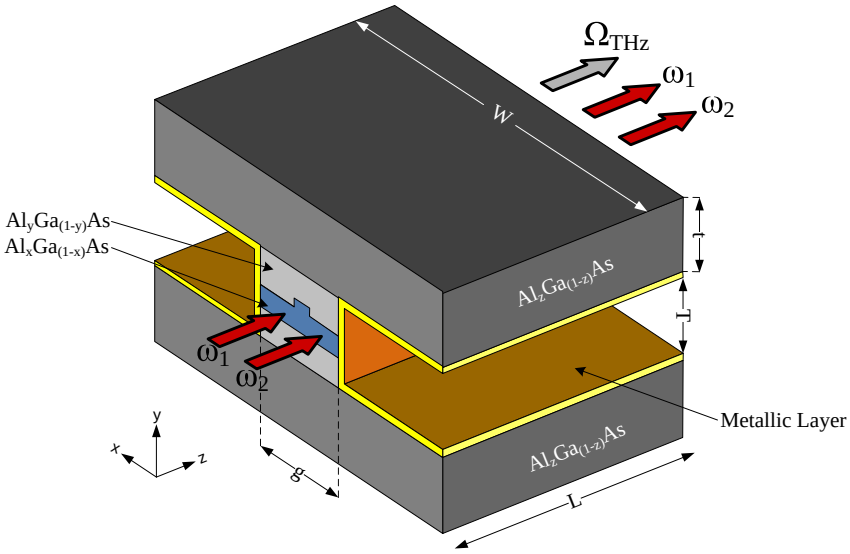

Figure 5.8: Integration of a dielectric ridged slab waveguide and a metallic slit waveguide for terahertz generation (g= 4.5μm, T= 5μm, ridge height= 1.25μm, ridge width= 1.1μm, x=0, y=0.2, z=0.4).

effective index.

An incident beam consisting two x-polarized optical frequencies of ω_1 and ω_2 is guided by the optical waveguide. The x direction is parallel to $< 111 >$ crystal direction which results in equal field magnitudes in all crystallographic axes. The isotropic nonlinear susceptibility of the GaAs crystal, as discussed in previous chapter, results in a difference-frequency signal generated by nonlinear interactions with the same magnitudes in all crystallographic axes, resulting in an x-polarized generated signal to be guided by the metallic slit waveguide. Accurate waveguide phase matching would let us extend the length of the device up to couple of centimeters to increase terahertz output powers.

The higher-order modes of the terahertz waveguide would have highly dispersive behavior, but are not expected to be important. Higher-order TE or TM modes confined in the slit area are not supported given the substantially sub-wavelength dimensions in terahertz regime. Other higher-order modes such as hybrid modes are not going to be excited significantly due to the overlap mismatch.

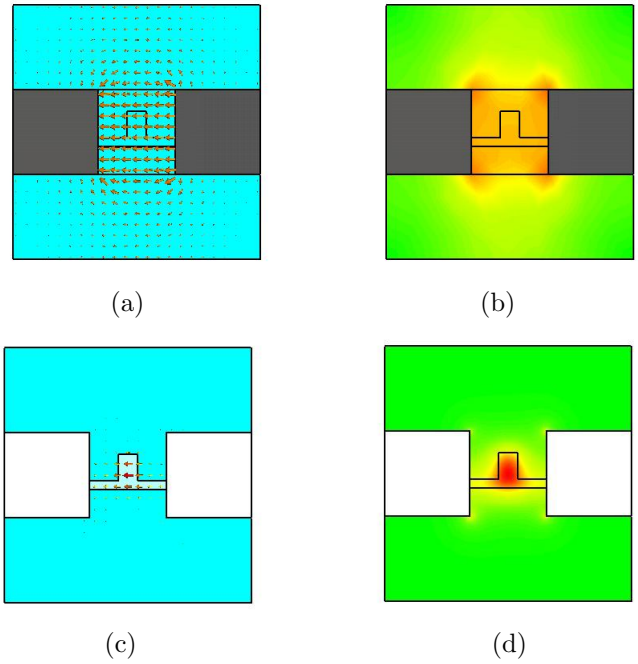

Figure 5.9: Electric field distribution of the fundamental modes in parallel-plate structure. (a) Field vectors at 2THz, (b) Field magnitude at 2THz, (c) Field vectors at 1.55μm, (d) Field Magnitude at 1.55μm.

The terahertz effective index and optical group index of the proposed device is depicted in figure 5.10 showing phase matching in the range of 0–3.5 THz by adjusting the optical wavelengths between 1.5–1.6 μm.

Figure 5.9 shows the electric field distribution of the optical and terahertz modes. The overlap between the normalized power distribution of the optical mode and the normalized electric field distribution of the terahertz mode is about 0.2 at 1.55 μm and 2 THz. For a 4-cm device, when the input pumps have power of 500 mW each, the output power is 0.56 mW according to equation 2.34. The output power can be enhanced by optimizing the dimensions of the waveguides.

Realization of the proposed device requires that it be fabricated with reasonable processing techniques and that the tolerances of this processing preserve accurate phase matching. This sensitivity can be estimated by exploring the effects of variations in refractive indices. The dependence of the output power on the phase mis-

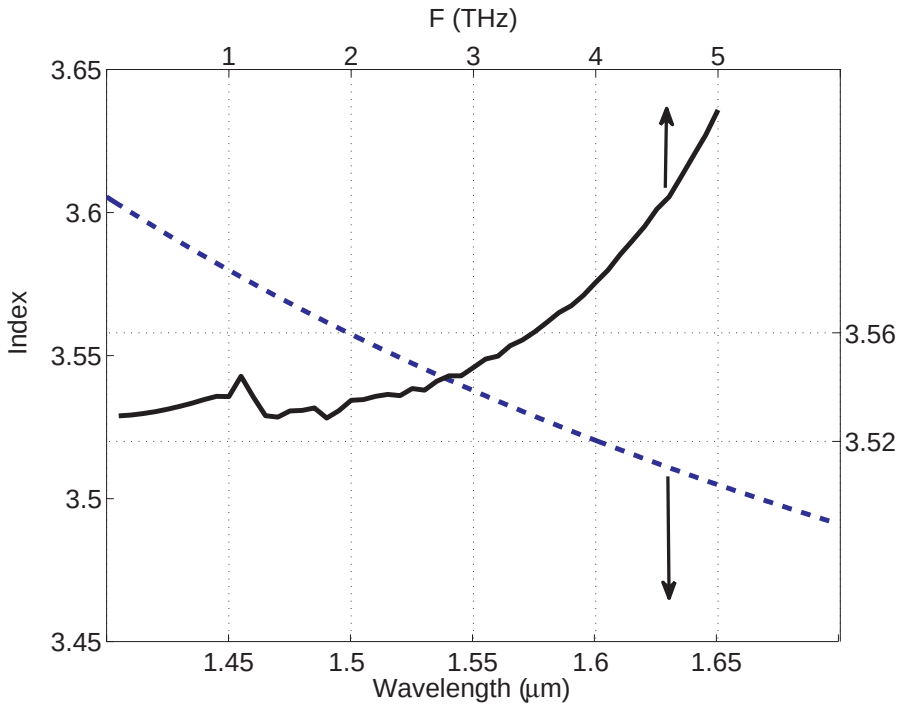

Figure 5.10: Terahertz effective index in comparison to the optical group index of the slit - slab structure.

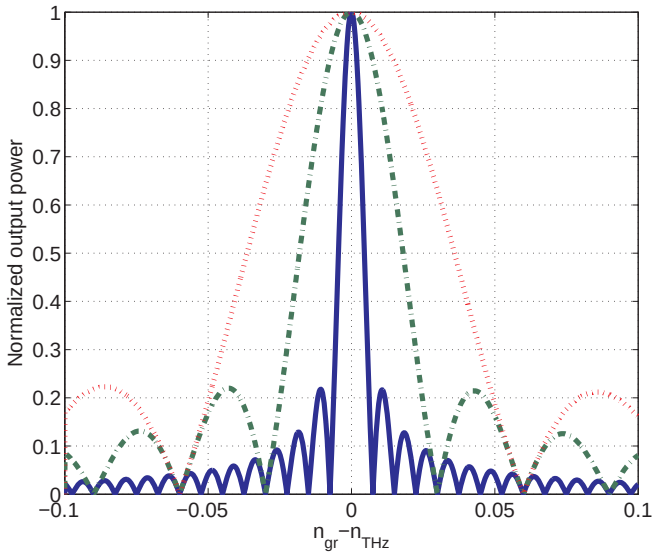

Figure 5.11: Phase mismatch for different device lengths (blue solid line: L=4 cm, green dash dot line: L=1 cm, red dash line: L=5mm).

match for different device lengths is depicted in figure 5.11. The figure shows that for L=4 cm, half maximum output power would be obtained even with the index mismatch of 0.005, which is more than 0.1% of the material refractive index.

5.5 Conclusion

In this chapter the performance of three devices are studied and discussed to be used for terahertz generation by difference-frequency mixing. The first device, parallel-plate structure, is used previously for optical modulation [52]. This device is studied as a terahertz source by desired DFG process. In the next two structures a metallic slit waveguide is used for terahertz wave. For device II, silicon is used to compensate index mismatch of terahertz and optical waves, however, due to lack of optical waveguiding the interaction length is limited and the conversion efficiency is very low. In the device III, the dimension of the structure is reduced which makes it suitable for microfabrication processes, and combination of AlGaAs and GaAs is used to compensate the index mismatch. Better conversion efficiency and higher terahertz bandwidth is obtained. The output power at 2THz is predicted to be 0.56 mW from a 4-cm long device. Since the terahertz wave is a guided single mode, it can be easily coupled to other waveguides or antennas. Moreover, the proposed waveguide phase matching can be useful for other types of devices using similar nonlinear phenomena, such as coherent detection, electro-optic modulation, and ultra-short pulse generation.

Chapter 6

Simulation of Nonlinear Interactions

6.1 Introduction

In this chapter a new tool is proposed for simulation of spatial second-order nonlinear interactions of guided waves based on modified one-dimensional finite-difference time-domain (1-D FDTD) calculations with an embedded nonlinear susceptibility tensor. Parallel 1-D engines are used to calculate three dimensional behaviors according to propagation properties of the waveguides. The method has been used successfully to simulate difference-frequency mixing in GaAs for terahertz generation, and could be applied to a wide range of problems that could not be solved easily by conventional methods.

Although studied extensively for decades, the design of novel components based on nonlinear optics still suffers from lack of accurate, fast, and comprehensive simulation tools. Finite-difference time-domain (FDTD) technique, as a general tool for simulation of Maxwell's equations, has attracted a great attention for decades due to the simplicity and acceptable accuracy offered by the presence of powerful computers [75]. The modification of this method to include nonlinear processes is challenging due to the computational overhead of switching between frequency and time domain implementation.

Approximations of frequency domain properties in time domain and using convo-

lution are of the main ideas that have been proposed for simulation of nonlinear interactions in FDTD. Simulation of second and third-order nonlinearities are added to FDTD using nonlinear Schrodinger equation in [76]. Another implementation of nonlinear FDTD is achieved using z-transform [77], and more recently, two dimensional implementation of FDTD for second and third-order nonlinearities is implemented [78]. All these methods work with scalar nonlinear coefficients and are limited to 43m symmetric crystals due to the absence of full tensor implementation. Also, the convolution based implementation adds significant computational overhead.

In this part, we propose a method based on simple modifications on 1-D FDTD for simulation of spatially dependent nonlinear interactions of guided modes. We show that, by using waveguide properties obtained by conventional simulation or analytical methods, we can exploit accuracy, and low computational expense of 1-D FDTD to calculate the three-dimensional nonlinear behaviors. The algorithm in this paper is presented for second order nonlinear processes such as difference and sum frequency generations, but could be modified to be used for higher-order effects. The proposed technique provides a powerful tool for dealing with frequency dependent properties of the waveguides and materials by calculating the multimode interactions in time-domain, which enables us to represent the properties associated with a valid frequency interval as a mode. We demonstrate this technique using terahertz generation by difference frequency mixing in GaAs and show good performance of the technique in comparison to analytical calculations.

6.2 Approach

The proposed 1D-FDTD procedure for simulation of guided waves with nonlinear interactions is based on two assumptions. We first assume negligible depletion of incident fields. This is usually valid because the magnitudes of the generated fields are much smaller than the magnitudes of the incident fields, due to small nonlinear co-

efficients. The second assumption is orthogonal propagation properties of waveguide modes. Coupling between the supported modes is neglected, except the nonlinear coupling. This is valid for single-mode waveguides and most multimode waveguides. According to the first assumption, the source fields and generated fields could be separated in the Maxwell's curl equations resulting in two set of new equations,

$$\frac{\partial \vec{B}_s}{\partial t} = -\nabla \times \vec{E}_s, \tag{6.1}$$

$$\varepsilon_r \varepsilon_0 \frac{\partial \vec{E}_s}{\partial t} + \sigma \vec{E} = \nabla \times \vec{H}_s, \tag{6.2}$$

$$\mu \frac{\partial \vec{B}_g}{\partial t} = -\nabla \times \vec{E}_g, \tag{6.3}$$

and

$$\varepsilon_r \varepsilon_0 \frac{\partial \vec{E}_g}{\partial t} + \frac{\partial P^{(NL)}}{\partial t} = \nabla \times \vec{H}_g, \tag{6.4}$$

Where $\vec{E}_s, \vec{B}_s, \vec{H}_s$ refer to the incident field values, and $\vec{E}_g, \vec{B}_g, \vec{H}_g$ refer to the generated fields. According to the orthogonal mode assumption, the solution for the first set of equations, which doesnt contain a nonlinear process, could be approximated by plane wave propagation of waveguide modes. The properties of these guided modes could be obtained either analytically or by conventional simulation tools, and could be used for calculation of the source field values in the direction of propagation at each time step. However, the solution to the second set of equations, equations 6.3, 6.4, for generated fields, is obtained using 1-D FDTD and considering the second term on the left hand side of equation 6.4 as a source term. This source term is

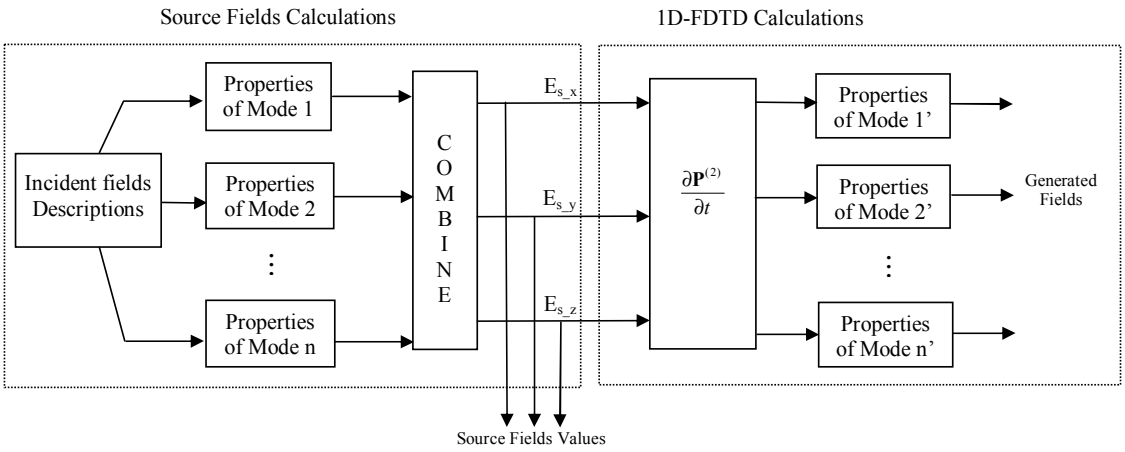

Figure 6.1: The schematic diagram of the proposed nonlinear FDTD. The mode properties of the waveguide or waveguides involved in the process should be computed separately.

calculated from the source field values given by:

$$\frac{\partial \vec{P}^{(2)}}{\partial t} = [T] \times \varepsilon_0 \begin{pmatrix} d_{11} & d_{12} & d_{13} & d_{14} & d_{15} & d_{16} \\ d_{21} & d_{22} & d_{23} & d_{24} & d_{25} & d_{26} \\ d_{31} & d_{32} & d_{33} & d_{34} & d_{35} & d_{36} \end{pmatrix} \times \begin{pmatrix} E_{x'}^2 \\ E_{y'}^2 \\ E_{z'}^2 \\ E_{y'}E_{z'} \\ E_{x'}E_{z'} \\ E_{y'}E_{x'} \end{pmatrix}, \tag{6.5}$$

where $E_{x'}, E_{y'}, E_{z'}$ are the components of electric field on the crystal axes and [T] is the matrix to transform the resulting polarization vector to the coordinate system used in equations 6.1-6.4.

Figure 6.1 shows the schematic diagram of the proposed method. For the source fields calculation part, we know the waveguide properties for the incident fields. Each mode properties block refers to a unique set of mode properties valid for a specific part of the incident signal. For example, if the incident signal contains two optical wavelengths that propagate with the fundamental mode of the optical waveguide but with different effective indices (due to dispersion), for each wavelength

a separate set of mode properties should be considered. The outputs of the combine block are the components of Es at each time step at all nodes in the direction of propagation. According to the computed source field values, the time derivative of nonlinear polarization is calculated by the backward difference method for all nodes, and it is fed to the 1-D FDTD calculations of all supported modes for the generated signals.

For each mode properties block for the generated waves in the waveguide, we consider a modified 1D-FDTD formulation. For example for the y-polarized field propagating in the x direction, the equations for updating the field values would be as following:

$$\mu \frac{H_z|_x^{t+\Delta t} - H_z|_x^t}{\Delta t} = -\frac{E_y|_{x+\frac{\Delta x}{2}}^{t+\frac{\Delta t}{2}} - E_y|_{x-\frac{\Delta x}{2}}^{t+\frac{\Delta t}{2}}}{\Delta x}, \tag{6.6}$$

and

$$\varepsilon_r \varepsilon_0 \frac{E_y|_{x+\frac{\Delta x}{2}}^{t+\frac{\Delta t}{2}} - E_y|_{x+\frac{\Delta x}{2}}^{t-\frac{\Delta t}{2}}}{\Delta x} + \frac{\partial \vec{P}^{(NL)}}{\partial t} = \frac{H_z|_{x+\Delta x}^t - H_z|_x^t}{\Delta t} \tag{6.7}$$

Where Δt is the time step and Δx is the mesh size. Electric field values, E_y, are calculated in positions starting from $\Delta x/2$ and at time steps starting from $\Delta t/2$. However, the magnetic field values are calculated at time steps and mesh steps starting from zero, to allow the central difference approximation for both time and space derivatives [75]. ε_r should be set as the effective dielectric constant of the corresponding mode. Loss of the modes also could be added to the equations when interpreted into effective electric or magnetic conductivities. The general equations for FDTD could be found in [75].

6.3 Results

To verify the ability of the proposed tool in simulation of second-order nonlinear interaction of guided waves, it has been used to simulate terahertz generation by difference frequency mixing in GaAs. In this example, perfect overlap between the modes is

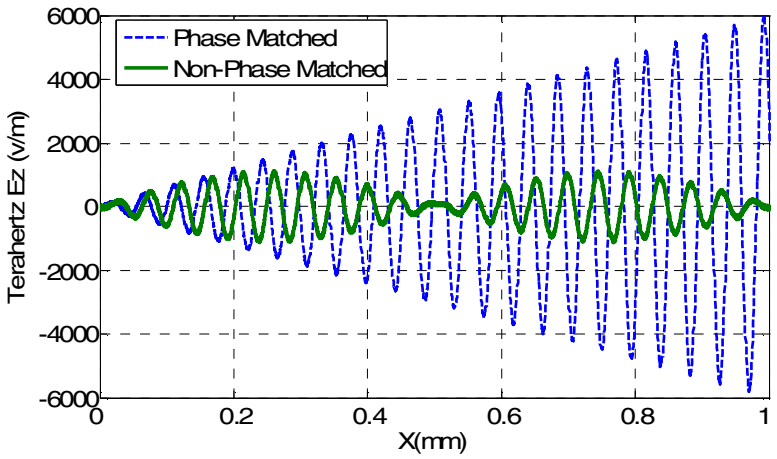

Figure 6.2: The generated terahertz signal at a certain time step for two cases of phase-matched and non-phase-matched environment (mesh size is $5 \times 10^{-7} m$).

assumed to simply acquire comparable results to theoretical calculations. Theoretical calculations are based on the plane wave approximation using the equations provided in chapter 2.

Two z-polarized optical wavelengths with the difference frequency of 2 THz and central wavelength of 1.55 μm have been applied to the waveguide. Considering the incident electric fields are parallel to $< 111 >$ direction of the crystal, the generated terahertz field values for all data points at a certain time step and for two cases of phase-matched and non-phasematched conditions are depicted in figure 6.2. The amplitude of the incident fields are 2.3×106 V/m, the group index for optical wavelengths is 3.4, and the effective index of the terahertz wave is 3.4 and 3.1 for phase-matched and nonphase- matched situations, respectively. The nonlinear FDTD method clearly reproduces the well known oscillatory behavior of difference frequency generation for non-phasematched condition, and the linear (in x) growth for phase-matched.

Figure 6.3 shows the comparison between the results obtained from the nonlinear FDTD method and theoretical calculation for terahertz generation in GaAs for perfect phase matching. The upper curves are for the crystal cut where the incident

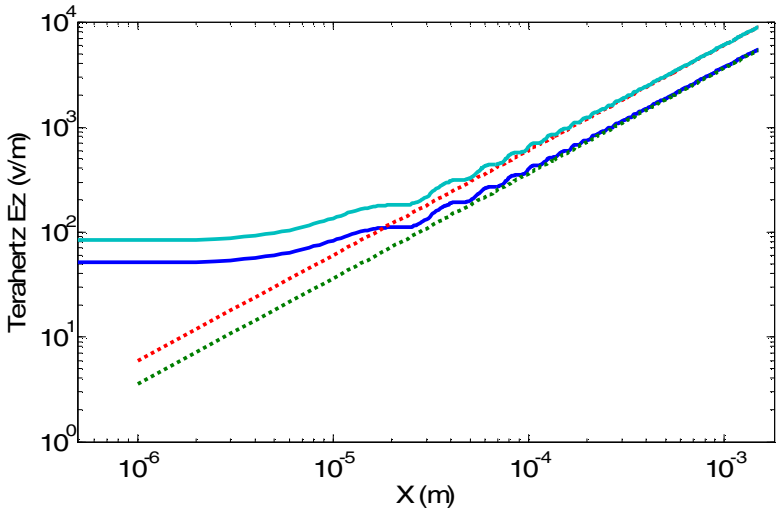

Figure 6.3: Generated terahertz electric field magnitude calculated by nonlinear FDTD (solid line) and theoretical calculations (dash line). The upper curve is for crystal cut in $< 111 >$ direction and the lower curve is for $< 110 >$ direction.

electric fields are parallel to the $< 111 >$ direction, and the lower curves are for fields parallel to the $< 110 >$ direction. The dependence on crystal orientation arises from transformation matrix [T] in equation 6.5, for nonlinear FDTD, and a different effective nonlinear coefficient for theoretical calculations.

The 1D cell size for FDTD is 5×10^{-7} m. The results obtained for the lengths containing few mesh cells are far from the expected values. However, after passing about 200 mesh cells (10^{-4} m) the difference become less than 2%. The logarithmic scale is used for both axes to magnify the error for short distances and small values of electric field. The resulting oscillations in amplitude and the initial error are partially due to the sudden excitation of the structure, and could be compensated when the incident fields are smoothly applied in time. Figure 6.4 shows the resulting electric field value in the y direction calculated in the $< 111 >$ case, showing calculation error of about 10^{-11} V/m.

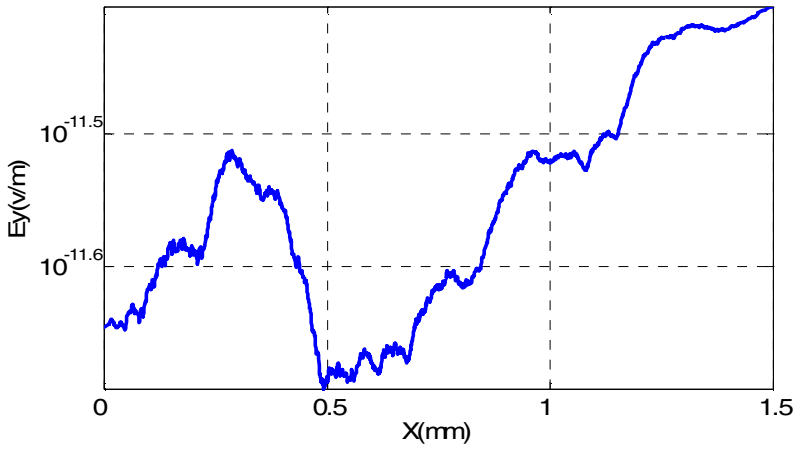

Figure 6.4: The calculated E_y field by nonlinear FDTD, which is supposed to be zero theoretically.

6.4 Discussion

The proposed method is based on a plane-wave approximation of the waveguide modes and electric field components of the modes which are perpendicular to the direction of waveguide. For TE and TEM modes, where the electric field is perpendicular to the direction of propagation, this approximation works well. However, for TM modes, there are two components of electric fields, one is perpendicular to and the other is in the direction of propagation. For lower-order modes, the component in the direction of propagation is much smaller than the transverse component and can be neglected with acceptable accuracy. To increase accuracy for calculation of the nonlinear polarizations involving TM source modes in equation 6.5, both components can be considered. For the generated TM modes, only the perpendicular component is calculated by FDTD and the other component is determined according to the ratio available in mode properties.

Conventional one-dimensional FDTD results in exact solution of Maxwell's equation [75], and it is always stable under the Courant criterion. In the nonlinear FDTD method, the stability depends on the added term of nonlinear polarization in equation 9. Since the nonlinear coefficients for materials are usually very small, this term

is regularly several orders of magnitude smaller than the other terms. No stability problem has been observed in cases considered.

Several nonlinear phenomena in which new frequencies are generated can be simulated with the proposed method, such as parametric amplification and oscillation, all-optical wavelength conversion, and electro-optic modulation. For other types of processes, such as soliton propagation, the algorithm should be modified to consider the effect of nonlinear processes on the incident signal (e.g. self-phase modulation), in addition to the generated signals. Overlap between the modes is an important issue that can be added to the method as appropriate coefficients to increase the accuracy.

6.5 Conclusion

In this chapter a new FDTD-based simulation tool is proposed to simulate three-dimensional nonlinear interactions of guided waves. The accuracy of the technique is verified in simulation of terahertz generation via difference frequency mixing. The proposed algorithm is simple, accurate and fast; hence it is an attractive method for the simulation and optimization of nonlinear waveguide components. Simulation of second and higher-order processes in grating-assisted waveguides, quasi-phase matched materials, and crystals with highly anisotropic tensor properties are potential applications of this method. These nonlinear processes are not easily incorporated into other conventional FDTD tools.

Chapter 7

Summary and Future Work

High power, tunable, coherent terahertz sources based on nonlinear difference-frequency generation are proposed. The phase matching is obtained for a wide range of terahertz frequencies, 0-3.5 THz, for a single device, while the input optical wavelengths are tuned in the range of 1.5-1.6 μm where lasers and amplifiers are widely available. The proposed terahertz source is expected to work in the mW range, while the input powers are 500mW each. This significantly high conversion efficiency compared to other DFG-based terahertz sources is obtained due to the high field strengths because of sub-wavelength dimensions of the device and long interaction length provided by wave-guiding. The output terahertz frequency is tuned by tuning the difference-frequency of the incident optical frequencies. While the difference-frequency is locked, the phase matching for the DFG process could be obtained by tuning the central frequency of the incident beams in the range of 1.5-1.6 μm.

The proposed devices are evaluated with numerical simulation of the waveguides and equations derived for nonlinear interactions of guided waves. The equations explaining the behavior of the DFG-based terahertz generation in a waveguide structure are derived based on the solution of Maxwell's equations in a nonlinear medium. CST Microwave Studio is used to simulate the behavior of waveguide structures, and effective index method combined with a one-dimensional mode solver is used to calculate

the effective index of the optical waveguides.

Three devices are proposed in this thesis for DFG-based terahertz generation. The first device, a combination of a parallel-plate waveguide and a dielectric slab waveguide, is a well-known structure for quantum cascade lasers. This device is studied as a terahertz source and the results show relatively high power output but very narrow band tuning range. The second device is a metallic slit waveguide in GaAs and silicon. Large terahertz tuning range is obtained but the output power is low due to the large dimension of the aperture and short interaction length due to the lack of optical wave-guiding. The third device is a combination of a metallic slit waveguide and a dielectric slab waveguide which resulted in a high power output and large tuning range for terahertz frequencies.

Although in this thesis the focus is on CW terahertz generation and DFG, the proposed devices could be used in applications such as efficient optical short pulse rectification, coherent detection and optical signal modulation. Second order nonlinearity of the device, and similar phase-matching conditions are needed for these applications. For optical rectification, when the applied electric field is a train of femtosecond pulses, the spectral bandwidth associated with such short pulses is in the terahertz range. The mixing of different frequency components, similar to DFG, produces a beating polarization, which results in the emission of electromagnetic pulses with terahertz frequencies. In optical modulation of a terahertz signal, the incident frequencies are an optical wavelength and a terahertz signal, and the second-order nonlinearity produces the optical side-bands based on DFG and SFG processes. The generated side-bands can also be used for detection of the incident terahertz signal. It means that the condition for interaction of optical and terahertz frequencies for many applications, such as what mentioned here, are very similar to the DFG-based terahertz generation and a device for one application can possibly be used for others with slight modifications.

The third device proposed in this thesis is expected to have an outstanding performance. However, fabrication of such device is still challenging. One of the main challenges is the ridge in the dielectric slab waveguide for lateral confinement of the optical mode. Although this is a standard structure for many laser diodes, it requires re-growth process which is challenging. As an alternative, for ease of fabrication, the lateral confinement also can be provided by deposition of a lower refractive index material such as glass.

The terahertz tuning range and the output power of the devices could be enhanced by optimizing the device dimensions. As it is discussed in the design chapter, both the tuning range and output power depend on the mode distributions and waveguide behavior. While it is a challenging multi-desciplinary optimization problem, the performance of each device could be enhanced using the proposed values as starting points.

Another possible modification to the proposed device is using more complex structures such as photonic crystals or slow-wave structures to tailor the phase-matching. The proposed simulation tool for modeling the nonlinear interactions can be used to comprehensively simulate the nonlinear behavior of the structures which is not easily achievable using conventional simulation and analytical methods.

The proposed FDTD tool in chapter 6 can be used for design of novel structures in which simulation and analyzing the nonlinear interactions are not straight forward. The tool can simulate generation of new frequencies and can be enhanced to be used for other nonlinear processes such as propagation of solitons.

Appendix A

Simulation Tools

Introduction

In this project we used two simulation tools to obtain the mode properties of the waveguide structures. For calculation of the effective and group index of optical waveguides, which are basically symmetric dielectric slab waveguides, combination of one dimensional mode solver and effective index method [63] is used. For calculating the field distribution of the optical modes, and all characteristics of terahertz modes, CST Microwave Studio [79] is used.

One-Dimensional Mode Solver

To decrease the simulation time for calculation of the mode properties of optical waveguide, we used a one-dimensional mode solver combined with effective index method. The one dimensional mode solver find the effective indices which satisfy equations 4.22 and 4.23 for a symmetric dielectric slab waveguide, and effective index method is an approximation of mode index for two dimensionally confined mode.

To find the solutions for equations 4.22 and 4.23, we used MATLAB. The equations are changed to find minima of a function in an interval. For exampel for the TE case, equation 4.22 can be written as:

$$\tan\left(\frac{k_0 d}{2}\sqrt{n_1^2 - n_{eff}^2} - (m-1)\frac{\pi}{2}\right) = \sqrt{\frac{n_{eff}^2 - n_2^2}{n_1^2 - n_{eff}^2}}, \quad m = 1, 2, 3, ... \tag{A.1}$$

which is:

$$\sqrt{\frac{n_{eff}^2 - n_2^2}{n_1^2 - n_{eff}^2}} - \tan\left(\frac{k_0 d}{2}\sqrt{n_1^2 - n_{eff}^2}\right) = 0, \quad \text{m:odd} \tag{A.2a}$$

$$\sqrt{\frac{n_{eff}^2 - n_2^2}{n_1^2 - n_{eff}^2}} + \cot\left(\frac{k_0 d}{2}\sqrt{n_1^2 - n_{eff}^2}\right) = 0, \quad \text{m:even} \tag{A.2b}$$

To find the n_{eff} values in the interval (n_2, n_1) which satisfy these equations, we discretize the interval and calculate the left sides of these equations. The positions in the interval that gives the minima peaks are close to the solutions. For further improvement of found results, "fmeansearch" function in MATLAB is used around the interval. Therefore, finding the effective indices of the TE modes in a symmetric dielectric waveguide would change into finding the minima of the following functions in the interval.

$$f_1(n_{eff}) = \log\left|\sqrt{\frac{n_{eff}^2 - n_2^2}{n_1^2 - n_{eff}^2}} - \tan\left(\frac{k_0 d}{2}\sqrt{n_1^2 - n_{eff}^2}\right)\right| \tag{A.3a}$$

$$f_2(n_{eff}) = \log\left|\sqrt{\frac{n_{eff}^2 - n_2^2}{n_1^2 - n_{eff}^2}} + \cot\left(\frac{k_0 d}{2}\sqrt{n_1^2 - n_{eff}^2}\right)\right| \tag{A.3b}$$

Figure A.1 shows the values of $f_1(n_{eff})$ and $f_2(n_{eff})$ for a symmetric dielectric waveguide where the core has refractive index of 1.5 and cladding has a refractive index of 1, for core thickness of 1.5λ. It shows that this waveguide supports four TE modes with the effective indices at which the minima of these function happened.

For each wavelength, the effective indices of the TM modes of a symmetric waveg-

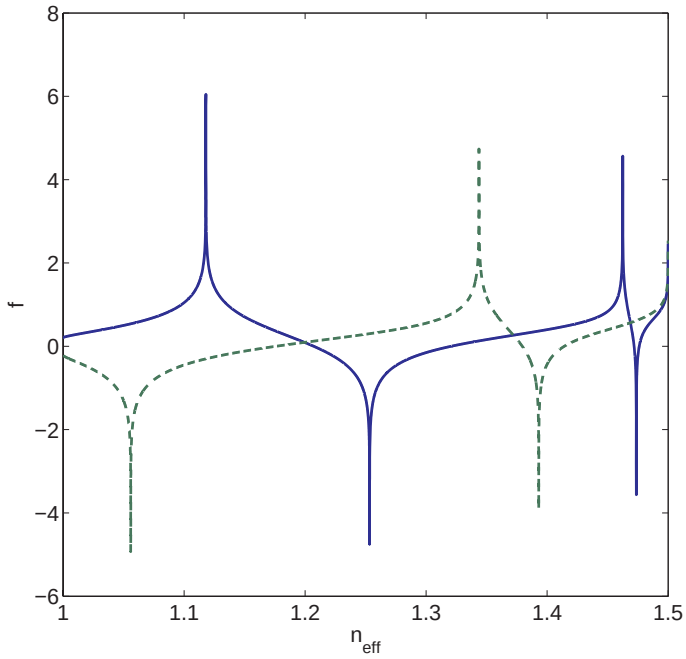

Figure A.1: $f_1(n_{eff})$ (blue - solid line) and $f_2(n_{eff})$ (green - dashed line) for a symmetric dielectric slab waveguide.

uide could be calculated similarly.

Effective Index Method

Effective index method [63] is an approximation technique for finding the effective index of the modes in a two dimensional dielectric waveguide. Because using a full-wave analysis for the optical waveguide in a wide range of frequencies is very time consuming on available computers, we used this approximation technique. Based on that the one dimensional mode solver is used to find the effective indices of a two dimensional waveguide.

CST Microwave Studio

CST Microwave Studio 2008 [79] is used for simulation of the terahertz waveguides as well as the field distribution of the optical waveguides. 2D mode solver of the frequency domain engine is used while the "adaptive tetrahedral mesh refinement" is on. For the meshing, in terahertz simulation 20 steps per wavelength is used

while the "material based refinement" is on, and for the optical range, 5 steps per wavelength without material based refinement. For the terahertz effective index of the waveguide in reported plots, a 100 GHz step is used. Plots and field distributions show reasonable simulation performance of this tool.

Bibliography

[1] R. W. Boyd, *Nonlinear Optics*. Academic Press, 2003.

[2] L. G. Cohen, W. L. Mammel, and S. Lumish, "Tailoring the shapes of dispersion spectra to control bandwidths in single-mode fibers," *Optics Letters*, vol. 7, no. 4, pp. 183–186, 1982.

[3] V. R. Kumar, A. George, W. Reeves, J. Knight, P. Russell, F. Omenetto, and A. Taylor, "Extruded soft glass photonic crystal fiber for ultrabroad supercontinuum generation," *Optics Express*, vol. 10, no. 25, pp. 1520–1525, 2002.

[4] H. Furukawa, A. Nirmalathas, N. Wada, S. Shinada, H. Tsuboya, and T. Miyazaki, "Tunable all-optical wavelength conversion of 160 Gb/s RZ optical signals by cascaded SFG-DFG generation in PPLN waveguide," *IEEE Photonics Technology Letters*, vol. 19, no. 6, pp. 384–386, 2007.

[5] J. D. Bull, N. A. F. Jaeger, H. Kato, M. Fairburn, A. Reid, and P. Ghanipour, "40 GHz electro-optic polarization modulator for fiber optic communications systems," in *Proc. SPIE*, vol. 5577, pp. 133–143, 2004.

[6] S. S. Dhillon, C. Sirtori, J. Alton, S. Barbieri, A. de Rossi, H. E. Beere, and D. A. Ritchie, "Terahertz transfer onto a telecom optical carrier," *Nature Photonics*, vol. 1, no. 411-415, 2007.

[7] W. Shi, Y. J. Ding, N. Fernelius, and K. Vodopyanov, "Efficient, tunable, and

coherent 0.18-5.27 THz source based on gase crystal," *Optics Letters*, vol. 27, no. 16, pp. 1454–1456, 2002.

[8] J. E. Schaar, K. L. Vodopyanov, and M. M. Fejer, "Intracavity terahertz-wave generation in a synchronously pumped optical parametric oscillator using quasi-phase-matched GaAs," *Optics Letters*, vol. 32, no. 10, pp. 1284–1286, 2007.

[9] G. Chang, C. J. Divin, J. Yang, M. A. Musheinish, S. L. Williamson, A. Galvanauskas, and T. B. Norris, "GaP waveguide emitters for high power broadband THz generation pumped by Yb-doped fiber lasers," *Optics Express*, vol. 15, no. 25, pp. 16308–16315, 2007.

[10] P. H. Siegel, "Terahertz technology," *IEEE Transactions on Microwave Theory and Techniques*, vol. 50, no. 3, pp. 910–928, 2002.

[11] M. Tonouchi, "Cutting-edge terahertz technology," *Nature Photonics*, vol. 1, pp. 97–105, 2007.

[12] R. E. Miles, P. Harrison, and D. Lippens, *Terahertz Sources and Systems*. Springer, 2001.

[13] F. C. DeLucia, *Sensing with terahertz radiation*, ch. Spectroscopy in the terahertz spectral regime, pp. 39–115. Springer, 2003.

[14] T. G. Phillips and J. Keene, "Submillimeter astronomy," *Proceedings of the IEEE*, vol. 80, no. 11, pp. 1662–1677, 1992.

[15] S. C. Chapman, A. W. Blain, R. J. Ivison, and I. R. Smail, "A median redshift of 2.4 for galaxies bright at submillimetre wavelengths," *Nature*, vol. 422, no. 695-698, 2003.

[16] M. R. Swain, "Options for studying star formation at high redshift," *Astronomical Society of the Pacific, Publications.*, vol. 110, no. 750, pp. 991–994, 1998.

[17] J.-M. Lamarre, "First (far-infrared and submillimeter space telescope): a major scientific project of esa," in *Proc. SPIE*, vol. 2019, pp. 267–274, 1993.

[18] P. F. Goldsmith, "The submillimeter wave astronomy satellite," in *IEEE MTT-S International Microwave Symposium*, pp. 395–398, 1991.

[19] H. M. Pickett, "THz spectroscopy of the atmosphere," in *Proc. SPIE*, vol. 3617, 1999.

[20] B. B. Hu and M. C. Nuss, "Imaging with terahertz waves," *Optics Letters*, vol. 20, pp. 1717–1718, 1995.

[21] D. Mittleman, M. Gupta, R. Neelamani, R. Baraniuk, J. Rudd, and M. Koch, "Recent advances in terahertz imaging," *Applied Physics B: Lasers and Optics*, vol. 68, no. 6, pp. 1085–1094, 1999.

[22] D. Crawley, C. Longbottom, V. P. Wallace, B. Cole, D. Arnone, and M. Pepper, "Three-dimensional terahertz pulse imaging of dental tissue," *Journal of Biomedical Optics*, vol. 8, no. 2, pp. 303–307, 2003.

[23] R. M. Woodward, B. E. Cole, V. P. Wallace, R. J. Pye, D. D. Arnone, and E. H. Linfield, "Terahertz pulse imaging in reflection geometry of human skin cancer and skin tissue," *Physics in Medicine abd Biology*, vol. 47, pp. 3853–3863, 2002.

[24] J. C. Dickinson, "Terahertz imaging of subjects with concealed weapons," in *Proc. SPIE*, vol. 6212, 2006.

[25] I. Mehdi, "Terahertz multiplier circuits," in *IEEE MTT-S International Microwave Symposium*, pp. 341–344, 2006.

[26] B. Ferguson and X.-C. Zhang, "Materials for terahertz science and technology," *Nature Materials*, vol. 1, pp. 26–40, 2002.

[27] M. Inguscio, G. Moruzzi, K. M. Evenson, and D. A. Jennings, "A review of frequency measurements of optically pumped lasers from 0.1 to 8 THz," *Journal of Applied Physics*, vol. 60, no. 161, 1986.

[28] C. W. Roberson and P. Sprangle, "A review of free-electron lasers," *Physics Fluids B*, vol. 1, no. 1, 1989.

[29] B. S. Williams, "Terahertz quantum-cascade lasers," *Nature Photonics*, vol. 1, pp. 517–525, 2007.

[30] J. Faist, F. Capasso, D. L. Sivco, C. Sirtori, A. L. Hutchinson, and A. Y. Cho, "Quantum cascade laser," *Science*, vol. 264, no. 5158, pp. 553–556, 1994.

[31] R. F. Kazarinov and R. A. Suris, "Possibility of the amplification of electromagnetic waves in a semiconductor with a superlattice," *Soviet Physics Semiconductors-USSR*, vol. 5, pp. 707–709, 1971.

[32] B. R. Pamplin, *Molecular Beam Epitaxy*. Elsevier, 1980.

[33] A. W. M. Lee, Q. Qin, S. Kumar, B. S. Williams, Q. Hu, and J. L. Reno, "High-power and high-temperature thz quantum-cascade lasers based on lens-coupled metal-metal waveguides," *Optics Letters*, vol. 32, no. 19, pp. 2840–2842, 2007.

[34] C. Baker, I. Gregory, M. Evans, W. Tribe, E. Linfield, and M. Missous, "All-optoelectronic terahertz system using low-temperature-grown InGaAs photomixers," *Optics Express*, vol. 13, no. 23, pp. 9639–9644, 2005.

[35] G. E. S. M. R. Brozel, ed., *Properties of Gallium Arsenide*. INSPEC, 1995.

[36] P. A. Franken, A. E. Hill, C. W. Peters, and G. Weinreich, "Generation of optical harmonics," *Physical Review Letters*, vol. 7, no. 4, pp. 118–119, 1961.

[37] A. Yariv, *Optical Electronics in Modern Communications*. Oxford, 1997.

[38] G. P. Agrawal, *Nonlinear Fiber Optics*. Academic Press, 1995.

[39] Y. J. Ding, "High power tunable terahertz sources based on parametric processes and applications," *IEEE Journal of Selected Topics in Quantum Electronics*, vol. 13, no. 3, pp. 705–720, 2007.

[40] K. L. Vodopyanov and P. G. Schunemann, "Efficient difference-frequency generation of 7- 20 μm radiation in CdGeAs2," *Optics Letters*, vol. 23, no. 14, 1998.

[41] M. M. Fejer, G. A. Magel, D. H. Jundt, and R. L. Byer, "Quasi-phase-matched second harmonic generation: tuning and tolerances," *IEEE Journal of Quantum Electronics*, vol. 28, no. 11, 1992.

[42] A. S. Kewitsch, M. Segev, and A. Yariv, "Tunable quasi-phase matching using dynamic ferroelectric domain gratings induced by photorefractive space-charge fields," *Applied Physics Letters*, vol. 64, no. 23, 1994.

[43] A. Bjarklev, J. Broeng, and A. S. Bjarklev, *Photonic Crystal Fibres*. Springer, 2003.

[44] F. Rahmatian, N. A. F. Jaeger, R. James, and E. Berolo, "An ultrahigh-speed AlGaAs-GaAs polarization converter usingslow-wave coplanar electrodes," *IEEE Photonics Technology Letters*, vol. 10, no. 5, pp. 675–677, 1998.

[45] A. Fiore, V. Berger, E. Rosencher, P. Bravetti, and J. Nagle, "Phase matching using an isotropic nonlinear optical material," *Nature*, vol. 391, 1998.

[46] C. A. Balanis, *Advanced Engineering Electromagnetics*. John Wiley and Sons, 1989.

[47] U. Peschel, K. Bubke, D. C. Hutchings, J. S. Aitchison, and J. M. Arnold, "Optical rectification in a travelling-wave geometry," *Physical Review A*, vol. 60, no. 6, pp. 4918–4926, 1999.

[48] B. Ainslie and C. Day, "A review of single-mode fibers with modified dispersion characteristics," *IEEE Journal of Lightwave Technology*, vol. 4, no. 8, pp. 967–979, 1986.

[49] T. Okuno, M. Hirano, T. Kato, M. Shigematsu, and M. Onishi, "Highly nonlinear and perfectly dispersion-flattende fibers for efficient optical signal processing applications," *IEEE Electronics Letters*, vol. 39, no. 13, pp. 972–974, 2003.

[50] S. J. B. Yoo, "Wavelength conversion technologies for WDM network applications," *IEEE Journal of Lightwave Technology*, vol. 14, no. 6, pp. 955–966, 1996.

[51] K. Wakita, *Semiconductor Optical Modulators*. Springer, 1998.

[52] J. Zhang, J. D. Bull, and T. E. Darcie, "Microwave photonic signal detection using phase-matched optical rectification in an AlGaAs waveguide," *IEEE Photonics Technology Letters*, vol. 19, no. 24, pp. 2012–2014, 2007.

[53] V. Loyo-Maldonado, H. K. Lee, C. R. Stanley, S. V. Rao, K. Moutzouris, M. Ebrahimzadeh, and J. S. Aitchison, "Generation of ultrashort electrical pulses in semiconductor waveguides," *IEEE Photonics Technology Letters*, vol. 15, no. 3, pp. 428–430, 2003.

[54] J. L'huillier, G. Torosyan, M. Theuer, Y. Avetisyan, and R. Beigang, "Generation of THz radiation using bulk, periodically and aperiodically poled lithium niobate – part 1: Theory," *Applied Physics B: Lasers and Optics*, vol. 86, no. 2, 2006.

[55] Y. J. Ding and W. Shi, "From backward THz difference-frequency generation to parametric oscillation," *IEEE Journal of Selected Topics in Quantum Electronics*, vol. 12, no. 3, pp. 352–359, 2006.

[56] C. Weiss, G. Torosyan, Y. Avetisyan, and R. Beigang, "Generation of tunable narrow-band surface-emitted terahertz radiation in periodically poled lithium niobate," *Optics Letters*, vol. 26, no. 8, pp. 563–565, 2001.

[57] G. Imeshev, M. E. Fermann, K. L. Vodopyanov, M. M. Fejer, X. Yu, J. S. Harris, D. Bliss, and C. Lynch, "High-power source of THz radiation based on orientation-patterned GaAs pumped by a fiber laser," *Optics Express*, vol. 14, no. 10, pp. 4439–4444, 2006.

[58] J.-I. Nishizawa, K. Suto, T. Tanabe, K. Saito, T. Kimura, and Y. Oyama, "THz generation from GaP rod-type waveguides," *IEEE Photonics Technology Letters*, vol. 19, no. 3, 2007.

[59] M. Balkanski and R. F. Wallis, *Semiconductor Physics and Applications*. Oxford, 2000.

[60] S. Adachi, *Properties of Aluminium Gallium Arsenide*. IET, 1993.

[61] S. Namba, "Electro-optical effect of zincblende," *Journal of the Optical Society of America*, vol. 51, no. 1, p. 76, 1961.

[62] M. Wächter, M. Nagel, and H. Kurz, "Metallic slit waveguide for dispersion-free low-loss terahertz signal transmission," *Applied Physics Letters*, vol. 90, no. 6, 2007.

[63] L. A. Coldren and S. W. Corzine, *Diode Lasers and Photonic Integrated Circuits*. John Wiley and Sons, 1995.

[64] M. Goto, A. Quema, H. Takahashi, S. Ono, and N. Sarukura, "Teflon photonic crystal fiber as terahertz waveguide," *Japanese Journal of Applied Physics*, vol. 43, no. 2B, pp. 317–319, 2004.

[65] K. Wang and D. M. Mittleman, "Metal wires for terahertz wave guiding," *Nature*, vol. 423, no. 376-379, 2004.

[66] E. D. Palik, ed., *Handbook of Optical Constants of Solids*. Academic Press, 1998.

[67] R. K. Hoffmann, *Handbook of Microwave and Integrated Circuits*. Artech House, 1987.

[68] D. M. Pozar, *Microwave Engineering*. John Wiley and Sons, 1996.

[69] S. B. Cohn, "Slot line on a dielectric substrate," *IEEE Transactions on Microwave Theory and Techniques*, vol. 17, no. 10, pp. 768–778, 1969.

[70] S. B. Cohn, "Slot-line field components," *IEEE Transactions on Microwave Theory and Techniques*, vol. 20, no. 2, pp. 172–174, 1972.

[71] B. Williams, S. Kumar, Q. Hu, and J. Reno, "Operation of terahertz quantum-cascade lasers at 164 K in pulsed mode and at 117 K in continuous-wave mode," *Optics Express*, vol. 13, no. 9, pp. 3331–3339, 2005.

[72] M. rochat, M. Beck, J. Faist, and E. Oesterle, "Measurement of far-infrared waveguide loss using a multisection single-pass technique," *Applied Physics Letters*, vol. 78, 2001.

[73] B. E. A. Saleh and M. C. Teich, *Fundamentals of Photonics*. John Wiley and Sons, 1991.

[74] K. W. Gossen, J. A. Walker, L. A. D'Asaro, S. P. Hui, B. Tseng, R. Leibenguth, D. Kossives, D. D. Bacon, D. Dahringer, L. M. F. Chirovsky, A. L. Lentine, and D. A. B. Miller, "GaAs MQW modulators integrated with silicon CMOS," *IEEE Photonics Technology Letters*, vol. 7, no. 4, 1995.

[75] A. Taflove and S. C. Hagness, *Computational Electrodynamics: The Finite-Difference Time-Domain Method*. Artech House, 2005.

[76] R. M. Joseph and A. Taflove, "Fdtd maxwell's equations models for nonlinear electrodynamics and optics," *IEEE Transactions on Antennas and Propagation*, vol. 45, no. 3, pp. 364–374, 1997.

[77] D. M. Sullivan, "Nonlinear fdtd formulations using z transforms," *IEEE Transactions on Microwave Theory and Techniques*, vol. 43, no. 3, pp. 676–682, 1995.

[78] C. M. Reinke, A. Jafarpour, B. Momeni, M. Soltani, S. Khorasani, A. Adibi, X. Yong, and R. K. Lee, "Nonlinear finite-difference time-domain method for the simulation of anisotropic, $\chi^{(2)}$, $\chi^{(3)}$ optical effects," *IEEE Journal of Lightwave Technology*, vol. 14, no. 4, pp. 480–492, 2002.

[79] Computer Simulation Technology, *CST Microwave Studio 2008 User's Manual*, 2008.